Sensitivity of Australian rainfall to driving SST datasets in a variable-resolution global atmospheric model

Ying Lung Liu[1,2], Lisa V. Alexander[1,2], Jason P. Evans[1,2], Marcus Thatcher[3]

[1] Climate Change Research Centre, UNSW Sydney, Sydney, New South Wales, Australia

[2] ARC Centre of Excellence for Climate Extremes, UNSW Sydney, Sydney, New South Wales, Australia

[3] CSIRO Environment, Commonwealth Scientific and Industrial Research Organisation, Aspendale, Victoria, Australia

Corresponding author: Ying Lung Liu (ying_lung.liu@unsw.edu.au)

Key Points:

- Model simulations that perform well on minimum standard metrics are not necessarily preferable for end-users with specific purposes.
- More versatile metrics are essential in benchmarking simulations for specific fields of research.
- Resolution of the driving sea surface temperature is important to simulate Indian Ocean Dipole-rainfall variability over Australia.

Abstract

In this study, we employ the Conformal Cubic Atmospheric Model (CCAM), a variable-resolution global atmospheric model, driven by two distinct sea surface temperature (SST) datasets: the 0.25° Optimum Interpolation Sea Surface Temperature (CCAM_OISST) version 2.1 and the 2° Extended Reconstruction SSTs Version 5 (CCAM_ERSST5). Model performance is assessed using a benchmarking framework, revealing good agreement between both simulations and the climatological rainfall spatial pattern, seasonality, and annual trends obtained from the Australian Gridded Climate Data (AGCD). Notably, wet biases are identified in both simulations, with CCAM_OISST displaying a more pronounced bias.

Furthermore, we have examined CCAM's ability to capture El Niño-Southern Oscillation (ENSO) and Indian Ocean Dipole (IOD) correlations with rainfall during Austral spring (SON) utilizing a novel hit rate metric. Results indicate that only CCAM_OISST successfully replicates observed SON ENSO- and IOD-rainfall correlations, achieving hit rates of 86.6% and 87.5%, respectively, compared to 52.7% and 41.8% for CCAM_ERSST5. Large SST differences are found surrounding the Australian coastline between OISST and ERSST5 (termed the "Coastal Effect"). Differences can be induced by the spatial interpolation error due to the discrepancy between model and driving SST. An additional CCAM experiment, employing OISST with SST masked by ERSST5 in 5° proximity to the Australian continent, underscores the "Coastal Effect" has a significant impact on IOD-Australian rainfall simulations. In contrast, its influence on ENSO-Australian rainfall is limited. Therefore, simulations of IOD-Australian rainfall teleconnection are sensitive to local SST representation along coastlines, probably dependent on the spatial resolution of driving SST.

Plain Language Summary

In this research, the Conformal Cubic Atmospheric Model (CCAM), a global atmospheric model, is used to study the impact of different driving sea surface temperature (SST) datasets on Australian rainfall simulations. Two SST datasets, one with high resolution (OISST) and another at lower resolution (ERSST5), are employed to drive CCAM (CCAM_OISST and CCAM_ERSST5). Model performance is evaluated using a benchmarking approach, indicating that both SST-driven experiments are in good agreement with observed rainfall patterns in Australia. However, both simulations exhibit wet biases, with CCAM_OISST having a more noticeable bias.

The study assesses CCAM's ability to capture the correlation between El Niño-Southern Oscillation (ENSO) and Indian Ocean Dipole (IOD) with rainfall during Austral spring. Results reveal that CCAM_OISST performs better, replicating observed correlations more accurately than CCAM_ERSST5. The research identifies strong SST differences found between OISST and ERSST5 around the Australian coastline. An additional experiment underscores that this "Coastal Effect" plays an important role in simulating IOD-Australian rainfall correlations, while its impact on ENSO-Australian rainfall is limited. In conclusion, robust simulations of IOD-Australian rainfall teleconnection require an accurate representation of local SST, which is related to the spatial resolution of SST products driving the model.

Keywords: CCAM; Climate model evaluation; El Niño-Southern Oscillation (ENSO); Indian Ocean Dipole (IOD)

1 Introduction

Australia's vast geographical expanse, extending from the tropics to the mid-latitudes, gives rise to a remarkably diverse climate. In-depth investigations into Australian climate variability and future climate projections necessitate robust model simulations of rainfall patterns. This complexity is further shaped by the influential phenomena of the El Niño-Southern Oscillation (ENSO; Trenberth 1997) and the Indian Ocean Dipole (IOD; Saji et al. 1999), which exert pronounced effects on rainfall seasonality and interannual variability within the region.

During El Niño events, Australia is typically drier than average due to enhanced subsidence and elevated sea-level pressure over the western Pacific (Meyers et al. 2007, Wang and Hendon 2007, Cai et al. 2011). As reported by the Australian Bureau of Meteorology (BOM) (Australian Bureau of Meteorology 2021), El Niño tends to reduce rainfall, particularly during the winter-spring period, despite the peak of ENSO occurring around December. Moreover, El Niño is frequently associated with the onset of drought conditions, with severe droughts having been observed during the El Niño episodes of 1982, 1994, 2002, 2006, and 2015. Conversely, La Niña events typically correspond to increased rainfall and an elevated risk of flooding in Australia (e.g., Kotwicki and Allan 1998, Coates et al. 2014, Liu et al. 2018). Meanwhile, the Indian Ocean Dipole (IOD) influences Australia primarily through equivalent barotropic Rossby wave trains (Saji and Yamagata 2003, Cai et al. 2011, Gillett et al. 2022). Studies by Ashok et al. (2003) and Meyers et al. (2007) have documented a higher likelihood of reduced rainfall during the positive phase of IOD (pIOD). Ummenhofer et al. (2009) have suggested that negative IOD (nIOD) conditions favour increased moisture transport, resulting in heightened rainfall in southeastern Australia. Additionally, the influence of IOD on the Australian climate exhibits asymmetry, with the positive phase generally having a more substantial impact (Weller and Cai 2013a).

Climate model simulations are invaluable to help unravel the intricacies of ENSO/IOD rainfall teleconnections in Australia. These simulations offer a self-contained and comprehensive representation of the physical relationship between ENSO/IOD and rainfall, shedding light on the underlying mechanisms. Moreover, they serve as a crucial tool for investigating the interplay between ENSO/IOD-induced rainfall variations and various internal and external factors, such as the influence of climate modes in different ocean basins and anthropogenic emissions. However, climate models with coarse spatial resolutions often fail to accurately capture rainfall at regional scales (e.g., Rauscher et al. 2010, Chen et al. 2018, Huang et al. 2018). Meanwhile, it is crucial to acknowledge that running fine-resolution simulations with a General Circulation Model (GCM) comes with substantial computational costs. In response to this challenge, dynamical downscaling techniques have been introduced (Giorgi 2019).

Dynamical downscaling has emerged as a widely employed approach for investigating the teleconnections between ENSO/IOD and localized rainfall patterns (e.g., Boulard et al. 2013, Ratna et al. 2017, Whan and Zwiers 2017, Worku et al. 2018, Verma and Bhatla 2021, Safari et al. 2023). Regional Climate Models (RCMs) with typical resolutions higher than 30km are employed to simulate the atmosphere driven by reanalysis or general circulation model (GCM) outputs with coarser resolutions exceeding 100km. Dynamical downscaling of low-resolution GCM outputs has become prevalent for regional climate projection studies, such as the Coordinated Regional Climate Downscaling Experiment (CORDEX; Giorgi et al. 2015).

Nevertheless, it is crucial to recognize that dynamical downscaling introduces additional sources of uncertainty. These uncertainties stem from differences in the spatiotemporal resolutions, dynamical cores and parameterization schemes employed by the RCM and the driving GCM. These disparities can make it challenging to attribute specific sources of error and bias (Marbaix et al. 2003, Castro et al. 2005, Tapiador et al. 2020). Additionally, the teleconnection pathway from ENSO/IOD to Australian rainfall primarily unfolds outside of Australia, covering a vast expanse of the Earth, particularly involving air-sea interaction processes. Defining the RCM domain to cover only the Australian continent excludes some crucial processes that occur far from Australia and are still handled by coarse-resolution GCMs. This exclusion can impact the accuracy of simulating teleconnections. However, it is also challenging to reduce computational costs effectively when including both the Pacific Ocean and Indian Ocean basins in RCMs. Furthermore, it is worth mentioning that outcomes from dynamical downscaling concerning regional ENSO/IOD influences are occasionally unsatisfactory and can even yield counterintuitive responses of rainfall to ENSO/IOD events (e.g., Boulard et al. 2013, Verma and Bhatla 2021).

To harness the advantages of fine-resolution simulations using an RCM while maintaining a global-scale simulation simultaneously, GCMs with variable spatial resolution have been developed. One notable example is the Conformal Cubic Atmospheric Model (CCAM), which was developed by the Commonwealth Scientific and Industrial Research Organisation (CSIRO) in Australia (https://research.csiro.au/ccam). CCAM, an atmospheric GCM (AGCM), is the first model employing a gridding algorithm that projects the Earth's atmosphere onto the surface of a cube (McGregor 2005; Thatcher and McGregor 2011). This projection method offers the flexibility to set varying horizontal resolutions across the six faces of the cube, facilitating global simulations with different resolutions in various regions. As a result, finer resolutions can be established over the specific domain of interest, while the opposite side of the Earth, which is typically less relevant to the study, can have coarser resolutions. The variable-resolution feature matches the purpose of enabling a global simulation of ENSO and IOD and their teleconnections to rainfall characteristics over Australia while managing computational cost simultaneously.

CCAM has recently been used for climate projections in different Australian regions, including extreme weather projections developed by the National Environmental Science Programme's (NESP) Earth Systems and Climate Change Hub (ESCC Hub) and climate projections for the end of the 21^{st} century in Victoria, Tasmania, and Queensland for the government. CCAM has also been used in studies on the teleconnections between ENSO and regional weather (e.g., Chapman et al. 2020; Dechpichai et al. 2022) and long-term climate modelling (e.g., Katzfey et al. 2016; Nurlatifah et al. 2019; Toersilowati et al. 2022) in Southeast Asia. CCAM performs similarly to other RCMs in intercomparison assessments in Australia (Evans et al. 2016; Di Virgilio et al. 2019). Mantegna et al. (2017) show that CCAM can simulate extreme rainfall up to a 3-hourly scale. This gives us confidence that CCAM would be suitable for our study. However, most research has used CCAM as an RCM to downscale atmospheric data with coarser resolutions over a particular region based on global simulations with spatially varying resolutions. Recently, Gibson et al. (2023) evaluated CCAM as an AGCM in simulating New Zealand weather and climate. Their results showed that CCAM performed particularly well at simulating the variability and extremes of temperature and precipitation over New Zealand. Although they assessed CCAM's performance in simulating ENSO-precipitation patterns on a global scale during the Austral summer (DJF), there is a gap in the published evaluation of CCAM's performance in simulating the impact of ENSO on Australian rainfall during its most influential season, the Austral spring (SON), as specified by the Australian Bureau of Meteorology (2021).

Meanwhile, the performance of CCAM as an AGCM in the context of IOD-driven rainfall variability over Australia remains largely unexplored. This study aims to address this critical gap by conducting an evaluation of CCAM’s performance of Australian rainfall, including its response to the ENSO and IOD. Isphording et al. (2023) introduced a benchmarking framework for assessing climate models' ability to meet prior expectations. Our study has adopted the framework to see whether CCAM can meet the minimum standard of simulating Australia rainfall variability. It is noted that this framework was initially developed for dynamically downscaled GCMs with various RCMs and was demonstrated using simulations over Australia. Whereas we have employed their benchmarking framework for CCAM driven by observed SSTs. In addition to the minimum standard metrics, our study also introduces novel metrics to investigate ENSO- and IOD-related rainfall variability.

Various SST datasets with different timespan and data collecting methods are available for driving AGCM simulations. Longer-term SST products are preferred for investigating rainfall variability on scales beyond interannual patterns, such as ENSO- and IOD-driven rainfall. However, longer SST datasets often come with coarser spatial resolutions and increased uncertainty, particularly before the 1980s when satellite-based products were established. For instance, the Hadley Centre Sea Ice and Sea Surface Temperature data set (HadISST; Rayner et al. 2003), starting from 1871, has a fair spatial resolution of 1°× 1° which is comparable to a standard GCM simulation. It has been found to significantly underestimate IOD variability when compared to coral record-based SST reconstructions (see Pfeiffer et al. 2022). The Extended Reconstructed Sea Surface Temperature version 5 (ERSST5; Huang et al. 2017), with data available since 1854, is another well-known long-term SST dataset. It has a coarse spatial resolution of 2°×2°. While ERSST5 also tends to underestimate historical extreme positive IOD events, its IOD strength generally surpasses that of HadISST (Verdon-Kidd 2018, Pfeiffer et al. 2022). Moreover, ERSSTv5 gives the magnitude of the recent 2019 extreme pIOD more consistent with satellite-products (Ratna et al. 2021), while HadISST categorizes this event as a ‘moderate pIOD’. The advent of remote sensing via satellites in the 1980s led to SST datasets that blend satellite and in situ data, resulting in higher spatial and temporal resolutions. For instance, the daily NOAA Optimum Interpolation Sea Surface Temperature (OISST) version 2.1 (Huang et al. 2021) offers a 0.25°×0.25° grided daily dataset. Such satellite-based SST products tend to exhibit reduced uncertainty in ENSO and IOD variability when compared to interpolation-based datasets (Huang et al. 2016, Pfeiffer et al. 2022).

The accuracy of SST in proximity to the region of interest plays a pivotal role in the local teleconnection of ENSO and IOD events with rainfall patterns (Boulard et al. 2013). These SST values have a notable impact on smaller-scale atmospheric elements, including cumulus convection and the Madden-Julian Oscillation (MJO; Madden and Julian 1971, 1972) (Lim et al. 2021). The resolution of SST data has been identified as a critical factor affecting the performance of regional precipitation simulations (Cassola et al. 2016). A key issue arises when the resolution of the driving SST data is coarser than that of the model, resulting in a lack of SST values over model grid cells near coastlines. To address this, climate models resort to interpolation to estimate these missing values, which can lead to significant biases, particularly when temperature gradients are pronounced (Kara et al. 2008). Consequently, it is imperative to investigate the sensitivity of fine-resolution models, like CCAM, to the resolution and quality of the driving SST data in the context of ENSO and IOD-driven rainfall variability.

In this paper, we present an evaluation of CCAM's performance in simulating rainfall over Australia, utilizing the benchmarking framework proposed by Isphording et al. (2023). Our analysis aims to determine whether CCAM meets the predefined minimum standards. Additionally, we introduce innovative metrics to assess CCAM's performance in capturing the teleconnections between ENSO/IOD and Australian rainfall. Furthermore, we undertake a comparative analysis of CCAM simulations driven by different SST datasets to discern the model's sensitivity to the quality and resolution of the driving SST data.

2 Methodology

2.1 Model Experiments and Data Used

The research employed the Conformal Cubic Atmospheric Model (CCAM; McGregor and Dix 2008, McGregor 2015, Thatcher et al. 2023), version 2301, developed by the Commonwealth Scientific and Industrial Research Organisation (CSIRO), Environment Business Unit, Australia. Detailed documentation for CCAM can be accessed at https://research.csiro.au/ccam. CCAM utilizes a non-hydrostatic, semi-implicit, and semi-Lagrangian atmospheric dynamical core, alongside a hydrostatic, semi-implicit, and semi-Lagrangian ocean dynamical core. It also employs a reversible staggered grid to improve dispersion properties (McGregor 2005). The model incorporates an innovative mass-flux cumulus convection scheme, with its mathematical formulation elaborated in McGregor (2003). Subsequent versions of the scheme retained the same algorithm but underwent adjustments in parameters. Table 1 lists the other parameterisation schemes and model physics used, including surface models, aerosol models, radiation schemes, etc.

Simulation name	CCAM_OISST	CCAM_ERSST5
Simulation period	Sep 1981 – Dec 2022	Jan 1920 – Dec 2022
Model timestep	400s	
No. vertical levels	54	
Land surface model	CABLE (Kowalczyk et al. 2006), constant land-use	
Aerosol model	Prognostic aerosol (Rotstayn and Lohmann 2002, Rotstayn et al. 2011)	
Cloud microphysics	Lin et al. (1983) and Rotstayn (1997)	
Radiation	GFDL-AM4 radiation code with CMIP6 radiative forcings (Freidenreich and Ramaswamy 1999, Schwarzkopf and Ramaswamy 1999)	
Convective scheme	Mass-flux cumulus convection scheme (McGregor 2003), version mod2015a	
Atmosphere turbulent mixing	Hurley (2007)	
Gravity wave drag	Chouinard et al. (1986)	

Table 1. Configurations details and adopted parameterization schemes of CCAM simulations discussed in this study.

CCAM was the first three-dimensional atmospheric model to introduce the use of a cubic grid, known as the Conformal Cubic grid, which projects a sphere (i.e., the Earth's surface) onto a cube (McGregor 2005, Thatcher and McGregor 2011). This projection method allows users to set different horizontal resolutions across six faces of the cube, facilitating global simulations with variable resolutions in different geographical regions. Consequently, finer resolutions can be specified over regions of particular interest using a Schmidt coordinate transformation

(Schmidt 1977), while other less critical areas of the Earth can be simulated with coarser resolution, effectively reducing computational demand. In Figure 1, we illustrate the CCAM resolution configuration applied in our study. This grid system allows us to achieve higher resolutions over Australia (~20-30km), with lower resolutions over the tropical Pacific and Indian Ocean (~50-100km). This is important to enable rainfall to be well simulated over the continent while allowing a reasonable resolution for the two climate modes analysed in this study – ENSO and IOD. For regions such as the Atlantic, where fine resolutions are not a primary concern, a coarser resolution is run (~130-150km).

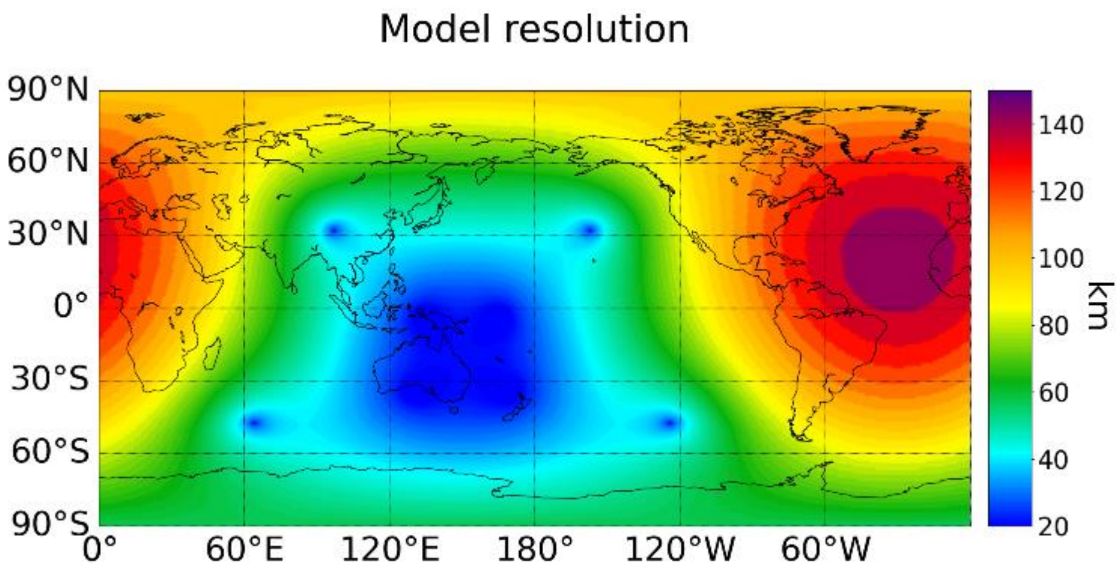

Figure 1. Spatial resolution (units: km) of CCAM simulations in this study.

In this study, CCAM operated as an Atmospheric General Circulation Model (AGCM) driven by two distinct sea surface temperature (SST) products. The first was the monthly NOAA Extended Reconstruction SSTs Version 5 (ERSST5; Huang et al. 2017) with a spatial resolution of 2.0°×2.0°, chosen for its suitability as a long-term, but relatively low-resolution SST dataset. The second was the daily NOAA Optimum Interpolation Sea Surface Temperature (OISST; Huang et al. 2021) version 2.1, offering a post-satellite-era high-resolution SST dataset at 0.25°×0.25° grid spacing. By comparing the simulation results driven by these two SST products, we aimed to explore the sensitivity of simulated rainfall over Australia to input SSTs. This examination also provides insights for striking a balance between longer temporal coverage and finer spatial details during model simulations. Alternative long-term SST datasets, such as the 1°x 1° Hadley Centre Sea Ice and Sea Surface Temperature (HadISST; Rayner et al. 2003) and the Centennial Observation-Based Estimates of SST (COBE; Ishii et al. 2005), were not considered due to their notable underestimation of IOD intensity when compared to OISST data and the reconstruction derived from reef records (Pfeiffer et al. 2022). For initializing CCAM simulations, we employed the ECMWF Reanalysis version 5 (ERA5) dataset (Hersbach et al. 2020), which was interpolated into a quasi-uniform cubic format.

The OISST driven run (CCAM_OISST) covered September 1981 to December 2022, while the ERSST5 driven run (CCAM_ERSST5) spanned from January 1920 to December 2022. Although these two integrations began at different times, the analysis in this study was based on data covering the period from December 1982 to November 2022, in order to provide ample time for the CCAM_OISST simulation to reach a stable state (spin-up). This timeframe encompassed 40 complete years, with an equal representation of each season. The details of the configurations and parameterization schemes used in the CCAM simulations for this study are listed in Tab. 1 and Thatcher and McGregor (2011).

In our study, model outputs were compared with observational data obtained from the Australian Gridded Climate Data version 1.0.1 (AGCD; Evans et al. 2020), specifically for rainfall and surface temperature. Additionally, atmospheric variables from ERA5 reanalysis data were used for comparison. Prior to the analysis, both the model output and observational/reanalysis datasets were interpolated to a common grid resolution of 0.25°×0.25° for Australia and 1°×1° for the entire globe, following standard latitudinal and longitudinal grid boxes. Subsequently, the rainfall and surface temperature datasets underwent further post-processing using Climpact, a tool developed by the World Meteorological Organization's (WMO's) Expert Team on Sector-Specific Climate Indices (ET-SCI) (Alexander and Herold 2016). This post-processing derived climate indices based on daily precipitation data to explore more "extreme" aspects of the precipitation distribution.

2.2 Evaluation of CCAM's performance

In our analysis, we assessed the performance of CCAM's rainfall output within a benchmarking framework, as proposed by Isphording et al. (2023). To determine whether CCAM met the minimum standards for rainfall simulations, we adopted the benchmark metrics recommended by Isphording et al. These metrics included: 1. mean absolute percentage error (MAPE) of annual mean rainfall 2. spatial correlation (SCor) for annual mean rainfall, 3. conformity of wet and dry season, and 4. significance of difference in Theil–Sen trends of annual rainfall in models and in the reference tested by corresponding p-value from the Mann-Kendall significance test (Hamed 2008). The computation and visualisation of these metrics are based on Isphording (2023).

The calculations for MAPE and SCor were performed following standard procedures commonly used in the field. To assess the conformity of wet and dry seasons, we determined whether the wettest and driest periods in each year in the model outputs coincided with those in the reference data. Theil–Sen trend is calculated by the median of $\frac{y_j - y_i}{x_j - x_i}$, where i and j represent different time points and $i \neq j$, to reduce the effect from outliers. The thresholds of the minimum standard metrics were set to $MAPE \leq 0.7, SCor \geq 0.75$ and the difference in Theil–Sen slopes at 0.1 significance level, as in Isphording et al. (2023).

In addition to the minimum standard metrics, our analysis encompassed several additional aspects to gain a comprehensive understanding of CCAM's performance in simulating rainfall variability (this is related to Isphording's versatility metrics within the benchmarking framework). These aspects include rainfall seasonality, 12-month Standard Precipitation Index (SPI), and El Niño-Southern Oscillation (ENSO)/Indian Ocean Dipole (IOD)-rainfall correlation. For the seasonality, we have evaluated whether the spatial patterns of maximum rainfall month and seasonal rainfall amplitude in CCAM's runs match with those in AGCD, following Isphording et al. (2023). We have calculated the mean absolute deviation (MAD; units: month) of the maximum rainfall month as a metric for the phase, and spatial correlation for the amplitude. For ENSO/IOD-rainfall correlation, we focus on the correlation between monthly rainfall and the NINO3.4 index (Bamston et al. 1997) or the Dipole Mode Index (DMI; Saji et al. 1999). NINO3.4 index is defined as the standardised SST anomaly over the central-eastern equatorial Pacific (5°N-5°S, 120-170°W) indicating the ENSO variability; while DMI is defined as the standardised difference in SST anomaly between the tropical western Indian Ocean (50° E–70° E, 10° S–10° N) and the tropical south-eastern Indian Ocean (90° E–110° E, 10° S–0). To quantify the performance of CCAM in simulating ENSO/IOD-rainfall correlation, a sign function is introduced:

$$Sgn(r) = \begin{cases} 1, & r > c \\ 0, & -c < r < c, \\ -1, & r < -c \end{cases}$$

where r is the Pearson correlation coefficient between monthly rainfall and the corresponding index, and c is the critical value determined by the significance test for correlation coefficients at a 5% significance level. Then, we calculate a hit rate defined as:

$$Hit\ rate = \frac{\Sigma_{\mathrm{i}} w_i Hit(r_m,\ r_o)_i}{\Sigma_{\mathrm{i}} w_i |Sgn(r_o)_i|},$$

$and\ Hit(r_m, r_o)_i = \begin{cases} 1, & Sgn(r_m)_i \times Sgn(r_o)_i = 1 \\ 0, & otherwise \end{cases}$, where w is the area weight, subscripts i indicates a grid, while m and o represent model outputs and observations respectively. The hit rate, expressed on a scale from 0 (0%) to 1 (100%), represents the proportion of the area where the model output exhibits a significant correlation with the correct sign when such a correlation exists in the observation. Similarly, the false alarm rate, indicating the portion of the area where the model gives a significant correlation not found in the observation, is defined as follows:

$$False\ alarm\ rate = \frac{\Sigma_{\mathrm{i}} w_i FA(r_n,\ r_o)_i}{\Sigma_{\mathrm{i}} w_i (1 - |Sgn(r_o)_i|)},$$

and false alarm $FA\ (r_n,\ r_o)_i = \begin{cases} 1, & |Sgn(r_m)_i| - |Sgn(r_o)_i| = 1 \\ 0, & otherwise \end{cases}$. Therefore, the hit rate assesses the percentage of model areas that exhibited the same significant sign of ENSO/IOD-rainfall correlation as observed. Conversely, the false alarm rate measures the percentage of model areas that display significant correlations not observed in the reference data. This additional evaluation allows us to better understand the model's suitability for the specific application related to interannual rainfall variability.

3 Results

3.1 CCAM performance on Australian rainfall

Annual mean rainfall, seasonal cycle, and annual rainfall trend were assessed using the minimum standard metrics outlined in the benchmarking framework proposed by Isphording et al. (2023). These assessments were conducted using the Australian Gridded Climate Data (AGCD) for the period spanning December 1982 to November 2022.

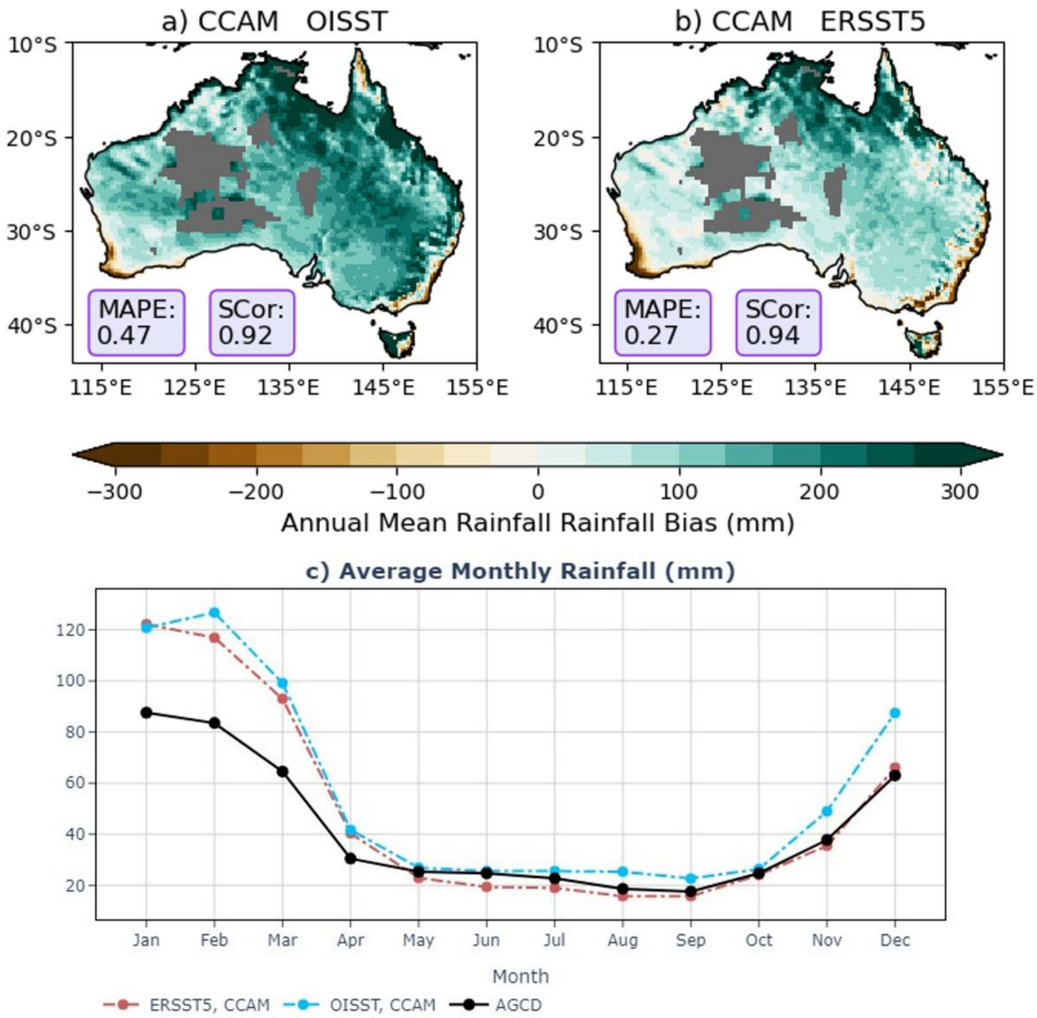

Figure 2. (a and b) Annual mean rainfall bias compared to AGCD (units: mm) for (a) CCAM_OISST and (b) CCAM_ERSST5. The mean absolute percentage errors (MAPE) and the weighted spatial correlation of the annual mean rainfall (SCor) are included in

the purple boxes (details are included in text). Grey shading masks areas without AGCD station data within a 0.5° proximity. Figure c is the monthly mean rainfall across Australia's land area (units: mm) for (black solid line) AGCD, (blue dash line) CCAM_OISST, and (red dash line) CCAM_ERSST5. The period of analysis spans from December 1982 to November 2022.

Figures 2a and 2b, the illustrate the annual rainfall bias of CCAM_OISST and CCAM_ERSST5, respectively. Generally, CCAM tends to simulate a wetter Australia, with a noticeable wet bias across most land areas for both model runs. However, it's worth noting that coastal areas in the southeast and southwest exhibit a dry bias. Importantly, the wet bias in CCAM_ERSST5, which is driven by coarser sea surface temperature (SST) data, appears to be less pronounced compared to CCAM_OISST. This leads to a smaller Mean Absolute Percentage Error (MAPE) for CCAM_ERSST5, although both MAPE values are relatively low, measuring less than 50%. In contrast to the wet bias, both CCAM_OISST and CCAM_ERSST5 demonstrate a high spatial correlation (SCor) in annual mean rainfall, with values exceeding 0.9. This high SCor suggests that the spatial pattern of annual rainfall in CCAM closely matches that observed in AGCD.

Figure 2c shows the analysis of average monthly rainfall over Australia in CCAM reveals a similar annual cycle to that observed in AGCD. In both CCAM runs and AGCD the wet season runs from November to April (NDJFMA) and the dry season from May to October (MJJASO). The model tends to overestimate rainfall during the wet season, particularly during December to March. In addition, CCAM_OISST shows a peak in average rainfall in February, while CCAM_ERSST5 and AGCD exhibit this peak in January.

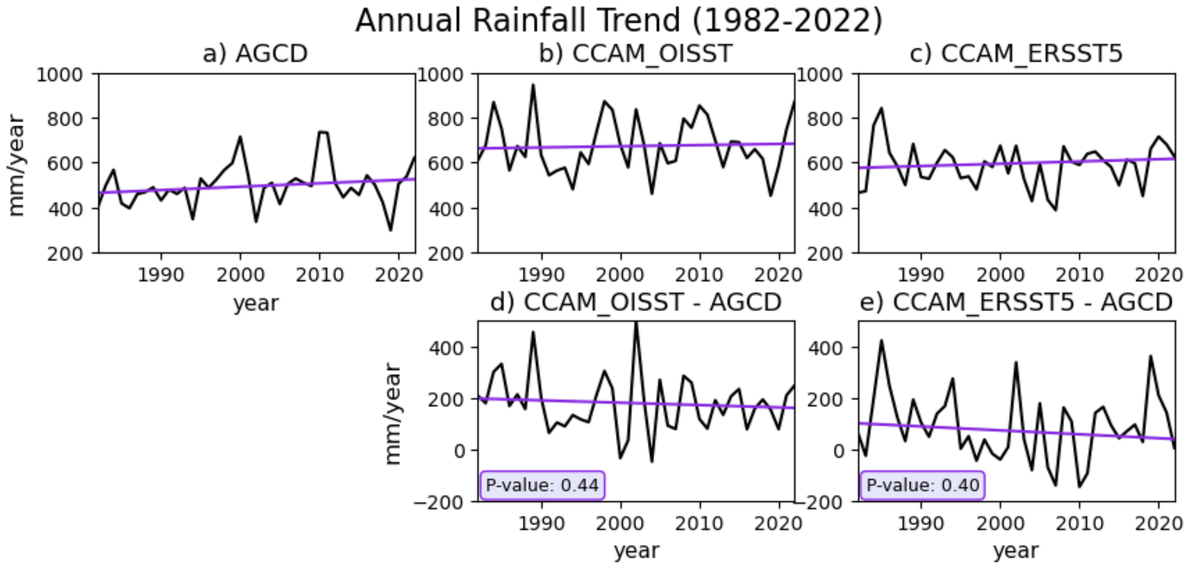

Figure 3. (a, b, c) (black solid lines) Annual rainfall time-series from 1982-2022 for (a) AGCD, (b) CCAM_OISST, (c) CCAM_ERSST5. The bottom panel shows the differences between (d) CCAM_OISST and (e) CCAM_ERSST5 and AGCD. The purple solid lines are the Theil–Sen estimators representing the trends. The p-values of Theil–Sen trends from Mann-Kendall significance test (Hamed 2008) are provided in the purple boxes for (d) and (e).

Both CCAM runs and AGCD exhibit a slight upward but not significant trend in rainfall over Australia (see Figs. 3a, 3b and 3c). Furthermore, despite AGCD giving a slightly stronger trend, no statistically significant trends are observed in the differences between the rainfall trends derived from CCAM runs and those from AGCD (Figs. 3d and 3e), with p-values around 0.4. Therefore, both simulations meet the minimum standard for the annual trend, thus satisfying all four minimum standard metrics.

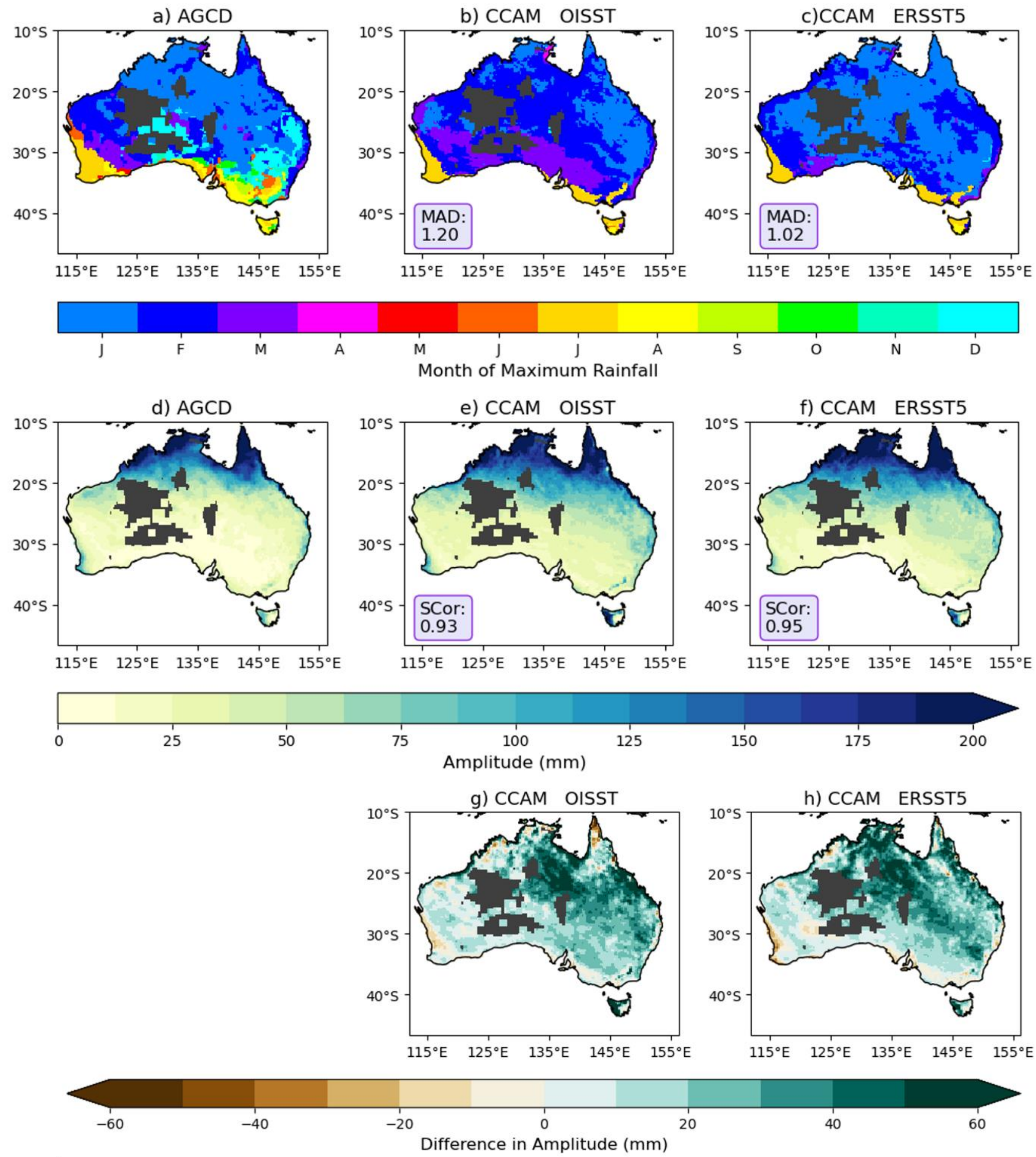

Figure 4. Spatial distribution of maximum rainfall month for (a) AGCD, (b) CCAM_OISST, and (c) CCAM_ERSST5. Each month is represented by a colour on the colour bar below the figure, from January (J) to December (D), indicating the corresponding month of maximum rainfall. Purple boxes display spatial weighted mean absolute deviations (MAD; units: month). Figures d, e and f are the climatological rainfall amplitude (units: mm), denoted by the range of average monthly mean rainfall,

for the same set of data. The corresponding weighted spatial correlations (SCor) are shown in the purple boxes. Grey shading masks areas without AGCD station data within a 0.5° proximity. Figures g and h are the differences in amplitudes between CCAM's outputs and AGCD for (g) CCAM_OISST minus AGCD and (h) CCAM_ERSST5 minus AGCD.

In addition to the minimum standard metrics, our analysis also considered the phase and amplitude of rainfall seasonality. Figure 4 presents maps of the month with the maximum average monthly rainfall (phase of rainfall seasonality) in the upper panel and the range of average monthly rainfall (amplitude) in the lower panel. In the case of AGCD, most regions in Australia experience their maximum rainfall during DJF, with some exceptions. The southwestern and southern coastal areas, as well as some inland areas in the southeast and Tasmania, typically have their rainfall peaks during JJA. The southeastern region exhibits a diverse distribution, with maximum rainfall occurring from July to December. Both CCAM_OISST and CCAM_ERSST5 generally align with AGCD in most northern and inland areas of Australia, where the maximum rainfall is correctly simulated to occur during DJF, consistent with AGCD. However, both model runs fail to reproduce the correct maximum rainfall month over the southeastern region. While they both show a confined area that peaks in July, outside this area they show a peak in rainfall in January or February, which is similar to other regions in Australia. This deviation from AGCD results in an average one-month displacement in the maximum rainfall month, with CCAM_OISST having a slightly larger deviation (1.20 months) than CCAM_ERSST5 (1.02 months). For the amplitude, both CCAM_OISST and CCAM_ERSST5 tend to overestimate the average monthly rainfall range across all regions in Australia. This overestimation is primarily due to an overestimation of DJF rainfall. Despite this, CCAM successfully reproduces a similar spatial pattern of seasonality amplitude compared to AGCD, with a high spatial correlation (SCor > 0.9) in both model runs. Although there are some deviations in the phase and amplitude of rainfall seasonality, both CCAM_OISST and CCAM_ERSST5 demonstrate reasonably good agreement with AGCD in most regions of Australia, highlighting CCAM's ability to capture rainfall seasonality irrespective of the driving SST dataset.

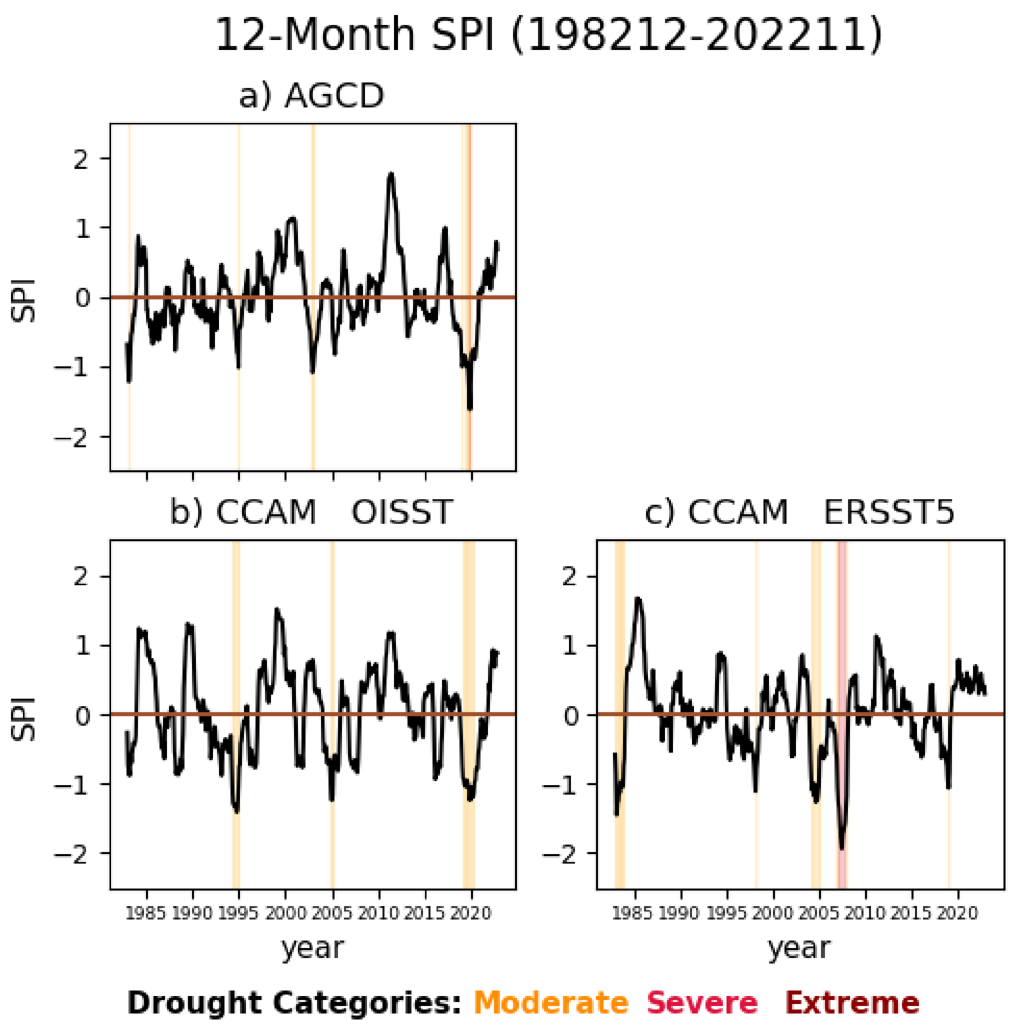

Figure 5. 12-month standard precipitation index (SPI; black solid lines) over Australia's land area (with the grids contain no station within a 0.5 proximity in AGCD masked) for (a) AGCD, (b) CCAM_OISST, and (c) CCAM_ERSST5. Drought categories, as defined by the World Meteorological Organization (WMO, 2012), are indicated by coloured vertical bars.

The evaluation of the 12-month Standard Precipitation Index (SPI), as shown in Figure 5, provides insights into the model's ability to capture historical drought events. Given that both runs are driven by observed Sea Surface Temperatures (SSTs), one would expect the timing of historical droughts to be similar between the simulations and AGCD. CCAM_OISST demonstrates the capability to reproduce a 12-month SPI time-series that coincides with AGCD, especially during events like the 2019 Black Summer (Davey and Sarre 2020). In contrast, CCAM_ERSST5 reproduces some drought events that are not present in AGCD, such as a severe drought in 2006-2007 and two long moderate droughts in 1983-1984 and 2004-2005. The difference observed between the two model runs in the 12-month SPI time-series suggests that CCAM_ERSST5 may perform less effectively in capturing interannual rainfall variability compared to CCAM_OISST. The interannual rainfall variability in Australia is largely influenced by teleconnections between large-scale climate drivers, such as ENSO and IOD, and local rainfall patterns. The divergence in performance between the two runs highlights the sensitivity of fine-resolution models like CCAM to the quality of the driving SSTs. Inaccurate representation of these SSTs can impact the model's ability to accurately simulate the teleconnections between climate drivers and rainfall, leading to discrepancies in the simulation of historical drought events.

In summary, both CCAM_OISST and CCAM_ERSST5 meet the minimum standards for regional rainfall simulations as proposed by Isphording et al. (2023) over Australia. They also exhibit good performance in capturing rainfall seasonality. However, when it comes to reproducing the 12-month Standard Precipitation Index (SPI) time-series, it is only CCAM_OISST that closely matches AGCD, suggesting a more accurate representation of historical drought events in higher-resolution SST-forced runs.

3.2 ENSO/IOD-related interannual rainfall variability

The examination of ENSO and IOD related monthly rainfall variability during the SON season provides insights into the differences between CCAM_OISST and CCAM_ERSST5 in capturing teleconnections between large-scale climate drivers and rainfall in Australia. Given the significant role of ENSO and IOD in influencing interannual rainfall variability, this analysis aims to uncover potential disparities between the two model runs and assess whether fine-resolution climate models are sensitive to the quality of driving SSTs when simulating these teleconnections, which operate on relatively longer timescales.

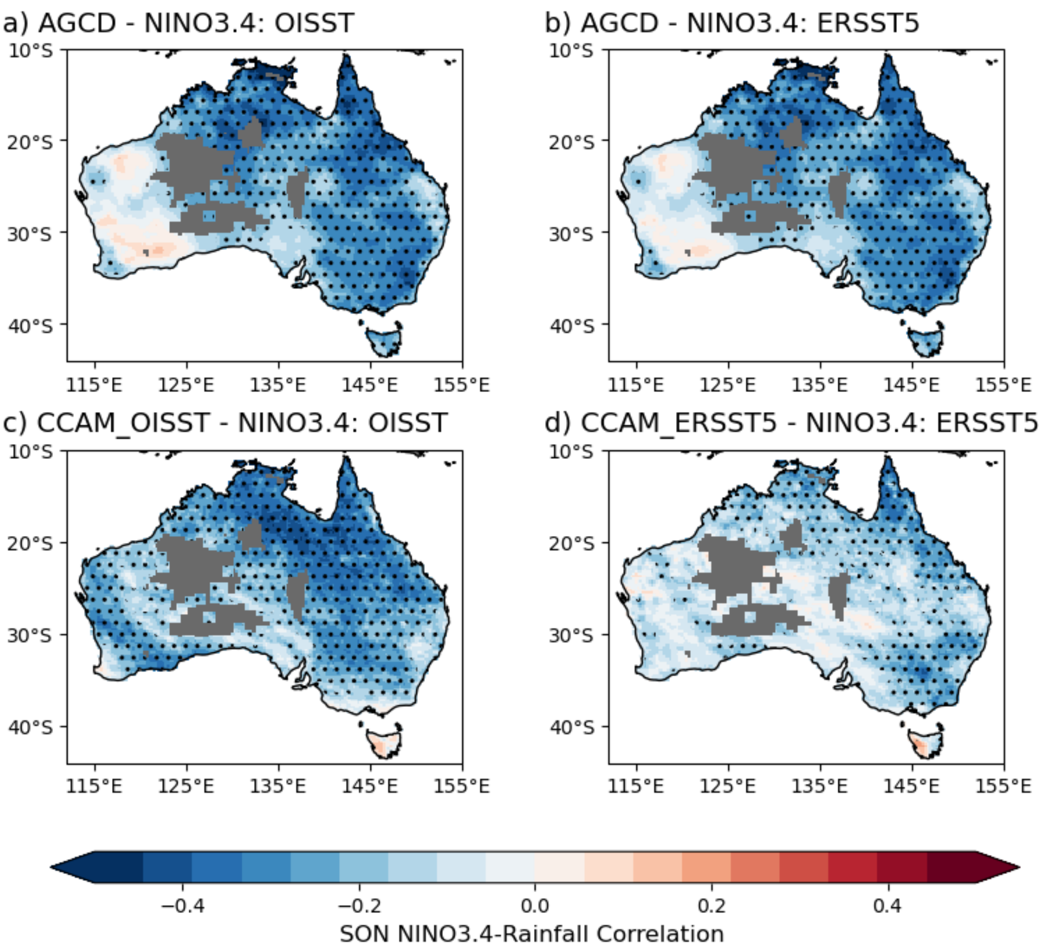

Figure 6. Correlations between linearly detrended SON monthly rainfall from (a, b) AGCD, (c) CCAM_OISST, (d) CCAM_ERSST5 and NINO3.4 from (a. c) OISST and (b, d) ERSST5, respectively. Dotted areas in the figure indicate grids with correlations that

are statistically significant at the 95% confidence level. Grey shading masks areas without AGCD station data within a 0.5° proximity.

ENSO and IOD are most effective during SON for Australia’s rainfall variability, so the analysis will focus on this season. Figure 6 displays the correlation between the NINO3.4 index and SON monthly rainfall for AGCD and CCAM runs. In AGCD, rainfall is mostly negatively correlated with NINO3.4 over the eastern and central regions of Australia, with correlation values around -0.4. Notably, there is no significant correlation observed over the western side of the country. CCAM_OISST generally agrees with AGCD by showing a negative correlation between NINO3.4 and rainfall over eastern and central Australia. However, it fails to reproduce the significant negative correlation along the southeastern coast and Tasmania seen in the observations. Interestingly, CCAM_OISST exhibits a significant negative correlation over the western side of Australia, a feature not present in AGCD. In contrast, CCAM_ERSST5 does not reproduce the significant negative correlation between NINO3.4 and rainfall over most land areas, with some exceptions in northern Australia and the southeast region. This indicates that the teleconnection between rainfall and ENSO is notably weaker in CCAM_ERSST5 compared to CCAM_OISST. The performance of the NINO3.4-rainfall correlation is quantified using a hit rate and false alarm rate. CCAM_OISST achieves a high hit rate of 0.866, while CCAM_ERSST5 lags behind with a hit rate of 0.527. However, CCAM_OISST also incurs a much higher false alarm rate of 0.705 compared to CCAM_ERSST5's lower false alarm rate of 0.173. This discrepancy is because CCAM_OISST tends to yield significant negative correlations across most of Australia, including regions where AGCD does not exhibit significant correlations. Conversely, CCAM_ERSST5 often produces no significant correlation, resulting in a lower false alarm rate. Given that there is a significant negative correlation over most of the land

(>75%) in AGCD, the hit rate takes precedence over the false alarm rate in this context. Consequently, CCAM_OISST outperforms CCAM_ERSST5 in reproducing the SON ENSO-rainfall correlation, indicating its better ability to capture ENSO's influence on rainfall during SON.

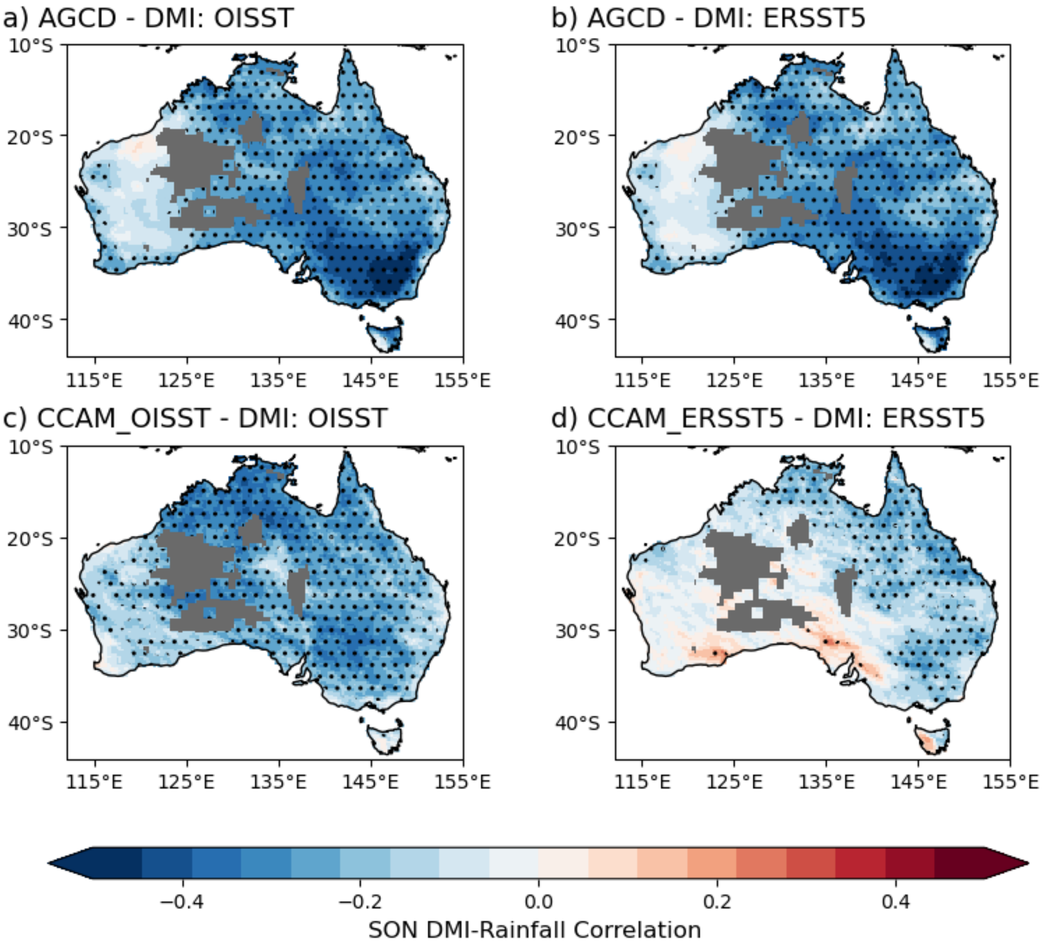

Figure 7. Same as figure 6, but for DMI.

The correlation between DMI and SON rainfall is shown in figure 7. AGCD exhibits a DMI-rainfall correlation pattern that is similar to the NINO3.4-rainfall correlation, with a strong negative signal (< -0.4) observed over the southeast region of Australia. CCAM_OISST generally agrees with AGCD in terms of the DMI-rainfall correlation, but it falls short in reproducing the strong negative correlation over the southeast region. While the correlation is significant in many areas, it is weaker than that observed in AGCD. Meanwhile, CCAM_ERSST5 fails to produce a significant DMI-rainfall correlation over most of the area. Only some locations in the northeast and southeast show weak correlations (around 0.2). CCAM_OISST achieves a high hit rate of 0.875, while CCAM_ERSST5 has a lower hit rate of 0.418. CCAM_OISST also has a higher false alarm rate (0.536) compared to CCAM_ERSST5. However, as with the ENSO-rainfall correlation analysis, the hit rate takes precedence in quantifying the performance of the IOD-rainfall correlation, given the significant negative correlation across most of the area in AGCD.

These results indicate that CCAM is capable of simulating the DMI-rainfall correlation well when driven by OISST, a high-resolution Sea Surface Temperature (SST) product. However, the correlation is significantly underestimated when CCAM is driven by ERSST5, which has a relatively coarse resolution. This underscores the sensitivity of fine-resolution climate models like CCAM to the quality and resolution of driving SST data when simulating teleconnections between climate drivers like IOD and regional rainfall patterns.

3.3 Sensitivity experiment: testing the impact on Australian rainfall of different driving SSTs

In order to understand the deficiency of CCAM_ERSST5 in reproducing the NINO3.4- and DMI-rainfall correlation, the difference between OISST and ERSST5 climatology after applying spatial interpolation by CCAM is examined. Prominent differences can be found over various regions, including western boundary currents such as the Kuroshio and Gulf Stream, as well as the Antarctic Circumpolar Current. Notably, there are substantial differences surrounding the Australian continent, with variations ranging from 0.5K to 1.0K, especially during JJA (Figs. 8a and 8b). Several factors contribute to these differences, including variations in data collection and post-processing methods. However, for values close to land, the resolution of the raw product plays an important role. ERSSTv5 has a resolution of 2°×2°, which is not fine enough to resolve values near the coastline. Consequently, when fine-resolution models like CCAM are driven by coarse-resolution SSTs, the model interpolates the SSTs to match its own resolution. This interpolation process involves statistically estimating SST values close to land based on surrounding SST data. When the SST gradient from the ocean to the land is strong, the interpolated SST values near land from a coarse-resolution product (e.g., ERSST5) deviate from the observed/measured values in a high-resolution product (e.g., OISST) significantly (hereafter referred to as the "Coastal Effect"). It also illustrates that the sign-switching of the difference between interpolated OISST and ERSST5 over northern Australia, where it is in general negative (positive) in JJA (DJF) when land is cooler (warmer) than ocean there, inducing a strong negative (positive) SST gradient towards land. The "Coastal Effect" might be a possible cause explaining why CCAM_OISST tends to produce wetter conditions than CCAM_ERSST5 over some regions surrounded by warmer OISST values. Warmer SST usually increases evaporation and convection, which can lead to enhanced rainfall. It is also suspected that this local SST difference in OISST and ERSST5 due to their resolution can be responsible for the distinction of the performance of ENSO/IOD-rainfall teleconnections.

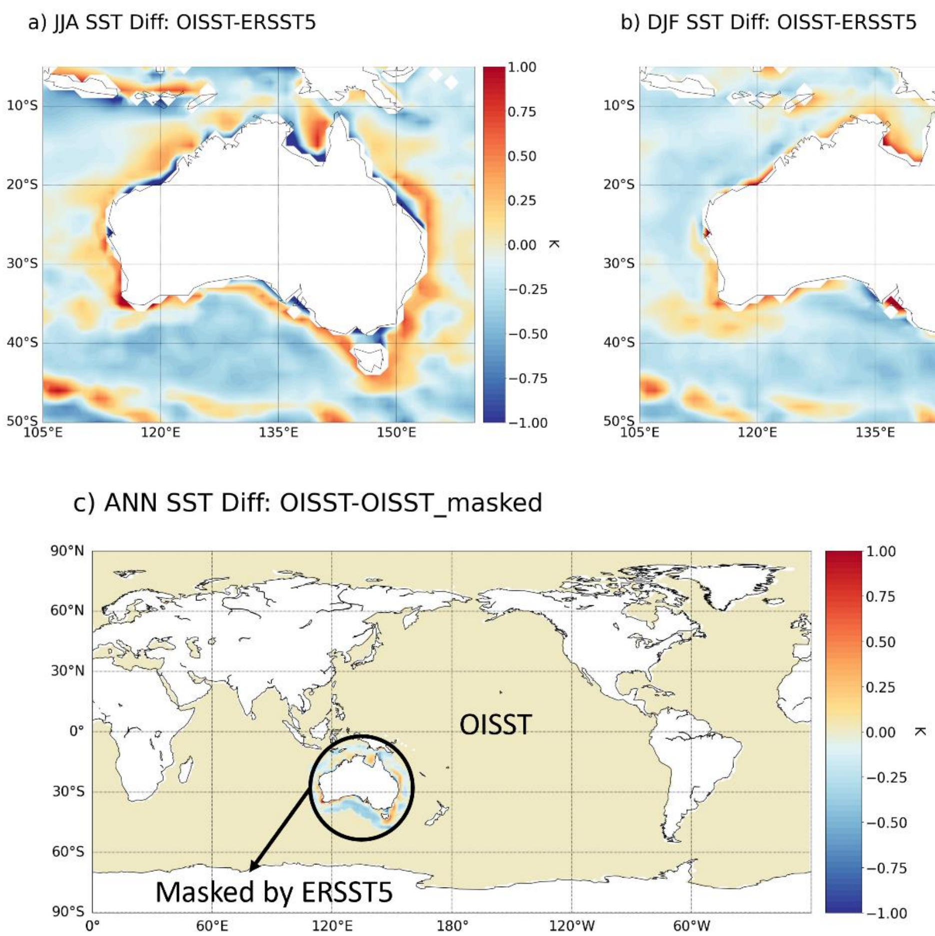

Figure 8. (a, b) Differencse between annual mean OISST and ERSST5 (units: K) after applying the spatial interpolation by CCAM in (a) JJA and (b) DJF. (c) is the difference between OISST and OISST_masked (units: K), which illustrates the experimental setup for CCAM_OISST_masked. In OISST_masked, sea surface temperatures surrounding Australia's land area are masked with temporally and spatially interpolated ERSST5, while all other regions remain consistent with OISST.

An experiment was conducted to investigate the impact of the "Coastal Effect" on the ENSO/IOD-rainfall teleconnection using CCAM. Initially, ERSST5 was temporally downscaled to daily resolution using the cubic interpolation method employed in CCAM. The daily ERSST5 was then spatially interpolated to a cubic grid with the same resolution as that used in CCAM_OISST and CCAM_ERSST5. The interpolated ERSST5 data were utilized to substitute the spatially interpolated OISST in the cubic grid over Australia. This modified SST dataset was employed to drive CCAM_OISST_masked (see Fig.8c as an illustration). Notably, CCAM_OISST_masked maintained all other settings identical to CCAM_OISST, with the sole distinction being the replacement of SST values surrounding the Australian continent (including Tasmania) with interpolated ERSST5 data within a 5° proximity.

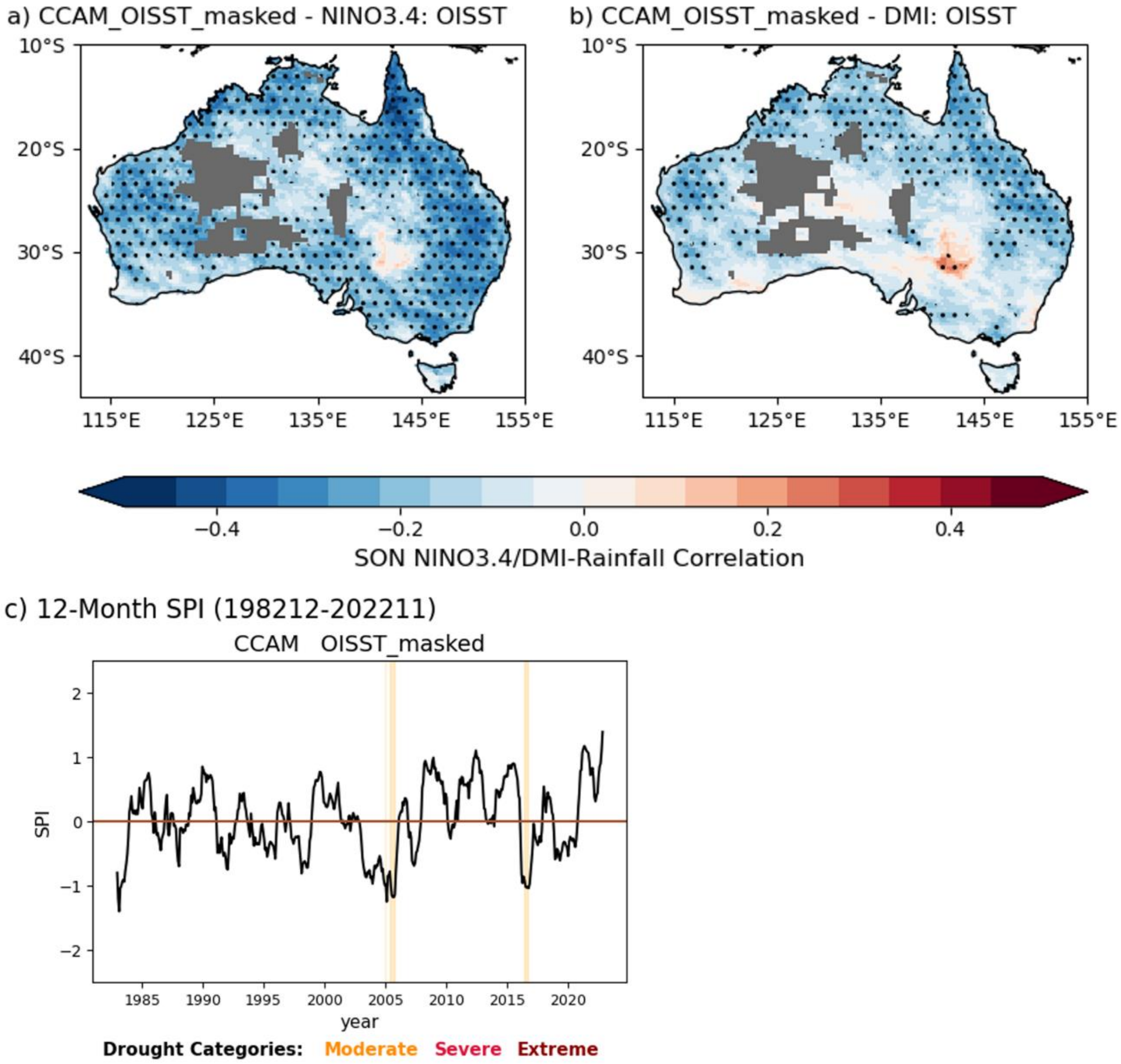

Figure 9. Correlations between linearly detrended SON monthly rainfall and (a) NINO3.4 and (b) DMI, respectively, from CCAM_OISST_masked. Dotted areas

highlight grids with statistically significant correlations at the 95% confidence level. Grey shading masks areas without AGCD station data within a 0.5° proximity. (c) is the 12-month SPI over Australia's land area (with the grids contain no station within a 0.5 proximity in AGCD masked) for CCAM_OISST_masked. Drought categories, defined by the WMO (2012), are indicated by coloured vertical bars.

The ENSO- and IOD-rainfall correlations in CCAM_OISST_masked during SON are depicted in Figs. 9a and 9b. CCAM_OISST_masked performs similarly to CCAM_OISST in terms of ENSO-related rainfall correlations, with regions displaying significant negative correlations in CCAM_OISST mostly being replicated in CCAM_OISST_masked (see Fig. 6c). The hit rate for CCAM_OISST_masked is 0.727, which falls between that of CCAM_OISST (0.866) and CCAM_ERSST5 (0.527) but is much closer to the former (see Tab. 2). This suggests that CCAM_OISST_masked can still produce satisfactory ENSO-rainfall teleconnections over Australia. The similarity between CCAM_OISST_masked and CCAM_OISST in SON ENSO-rainfall correlation indicates that the influence of SST on the ENSO-rainfall teleconnection is likely remote. The "Coastal Effect" and differences in SST resolutions have limited impact on the performance of ENSO-rainfall teleconnections in CCAM. In contrast, CCAM_OISST_masked exhibits a performance similar to CCAM_ERSST5 in IOD-related rainfall correlations. Both simulations yield weaker correlations compared to AGCD and CCAM_OISST. Notably, CCAM_OISST_masked does produce some significant negative correlations over the west of 120°E, which are not observed in CCAM_ERSST5. When compared to AGCD, CCAM_OISST_masked has a low hit rate of 0.402, which is much closer to CCAM_ERSST5 (0.418) than CCAM_OISST (0.875) (see Tab. 2). This indicates that masking the high-resolution SST data surrounding Australia with lower-resolution SST data can significantly affect the IOD-rainfall teleconnection in a fine-resolution model, even if conditions elsewhere remain unchanged. For the 12-month SPI (Fig. 9c), CCAM_OISST_masked fails to reproduce the 2019 drought like CCAM_ERSST5 (Fig. 5c). Conversely, it does not simulate the 2007 severe drought observed in CCAM_ERSST5. The 12-month SPI curve in CCAM_OISST_masked deviates significantly from both CCAM_OISST and CCAM_ERSST5. This suggests that the "Coastal Effect" can impact a fine-resolution model's ability to accurately simulate droughts.

	Hit Rate	
Runs	NINO3.4-Rainfall	DMI-Rainfall
CCAM_OISST	0.866	0.875
CCAM_ERSST5	0.527	0.418
CCAM_OISST_masked	0.727	0.402

Table 2. Hit rates for correlation (significant and correct sign) between NINO3.4 or DMI and SON monthly rainfall in CCAM simulations compared to AGCD.

In conclusion, the "Coastal Effect" emerges as an important factor influencing a fine-resolution model's ability to capture the IOD-rainfall teleconnection over Australia during SON. While ENSO-related rainfall teleconnections appear less affected by this Coastal Effect, the impact on IOD-related rainfall teleconnections can be significant, even if conditions elsewhere remain unchanged. Additionally, accurate drought simulations can also be affected by the Coastal Effect.

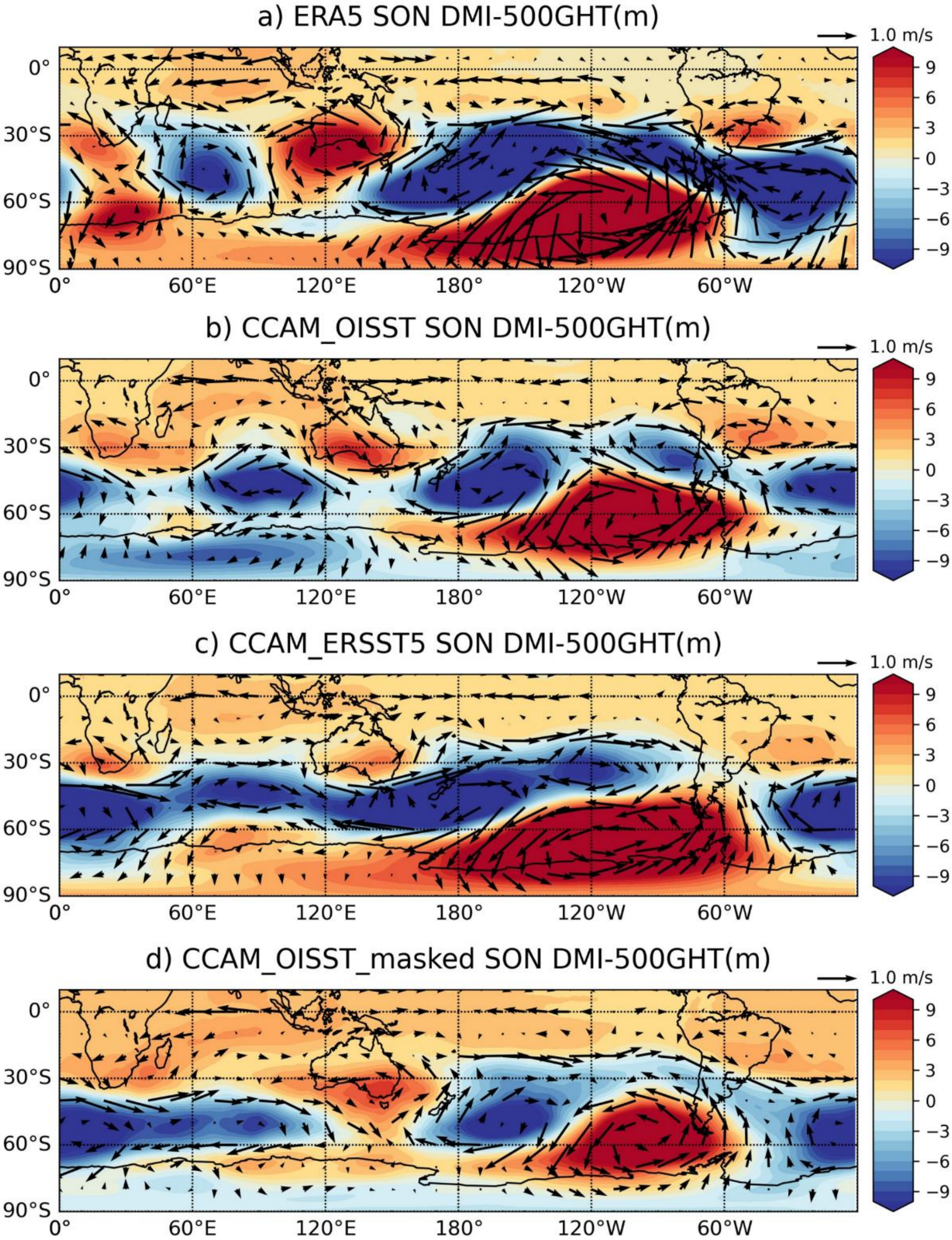

Figure 10. Covariance between DMI and linearly detrended 500-hPa geopotential height (shading, units: m) and wind (arrows, units: m/s) for (a) ERA5, (b) CCAM_OISST, (c) CCAM_ERSST5, and (d) CCAM_OISST_masked.

To investigate why IOD-rainfall teleconnection is heavily impacted by the "Coastal Effect", larger scale circulations associated with IOD are investigated. IOD remotely affects Australia through equivalent barotropic geopotential anomalies, commonly referred to as equivalent barotropic Rossby waves. These waves play a crucial role in transmitting IOD's influences through atmosphere and impacting regions at higher latitudes, including Australia (Saji and Yamagata 2003, Cai et al. 2011, Gillett et al. 2022). Figure 10 illustrates the covariance between DMI and 500hPa geopotential height (GHT) and wind for ERA5 and the three CCAM runs. A wavenumber 3 wave-like pattern is somewhat evident in ERA5 and CCAM runs, although it appears weaker in CCAM runs. This indicates that CCAM is capable of simulating how the IOD signal is transported to the atmosphere and influences regions at higher latitudes through the equivalent barotropic Rossby wave. The quasi-stationary positive 500hPa GHT anomaly over Australia is responsible for dry conditions during a positive IOD (pIOD) and wet conditions during a negative IOD (nIOD). However, the high-pressure anomaly is notably weaker in CCAM runs compared to ERA5, highlighting that CCAM generally produces a weaker IOD-rainfall correlation than observed. The difference in the high-pressure anomaly is further explored in Figure 11. CCAM_OISST exhibits a weaker and less extensive high-pressure anomaly compared to ERA5, resulting in a weaker IOD-induced rainfall response over southern Australia. CCAM_ERSST5, on the other hand, gives a weaker DMI-500hPa GHT covariance over western and southeast Australia than CCAM_OISST, further suppressing the IOD-rainfall response. In the case of CCAM_OISST_masked, the IOD-induced high-pressure anomaly and rainfall response are weaker than in CCAM_OISST over most of Australia. However, there is no substantial difference in the magnitude of the high-pressure anomaly between CCAM_OISST_masked and CCAM_ERSST5, except for significant positive differences over the southeastern and southwestern corners due to the displacement of low-pressure anomalies. These differences induce a stronger easterly wind from the ocean to southeastern Australia, transporting more moisture and suppressing the IOD's impact. Conversely, in the western part of Australia, stronger winds from the land enhance the IOD-rainfall correlation.

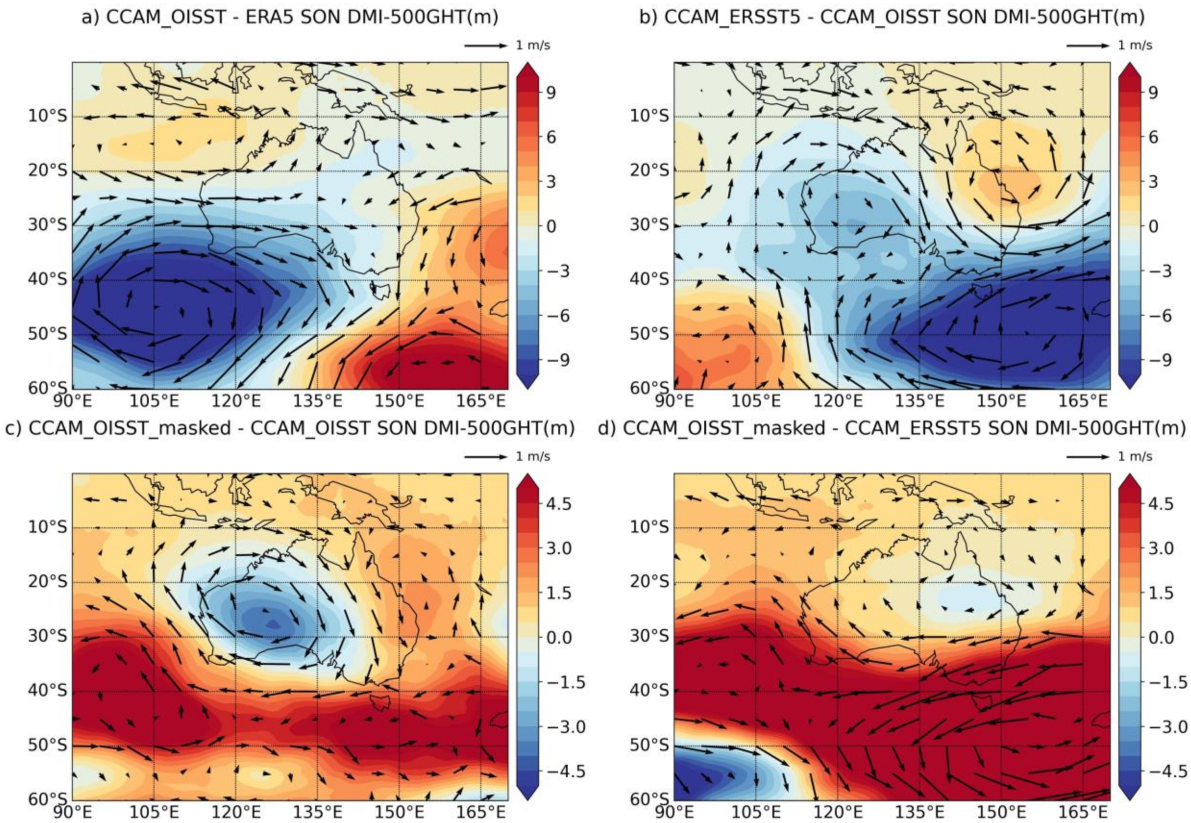

Figure 11. Differences in covariance between DMI and linearly detrended 500-hPa geopotential height (shading, units: m) and wind (arrows, units: m/s) for (a) CCAM_OISST minus ERA5, (b) CCAM_ERSST5 minus CCAM_OISST, (c) CCAM_OISST_masked minus CCAM_OISST, and (d) CCAM_OISST_masked minus CCAM_OISST5.

In summary, the "Coastal Effect" primarily affects the location and amplitude of the IOD-induced high-pressure anomaly over Australia, which, in turn, influences the local rainfall response. However, the precise dynamical mechanisms through which the "Coastal Effect" impacts the mid-level high anomaly require further investigation.

4 Discussion and Recommendation

4.1 Interpretation of the results within the benchmarking framework

This study has shown that CCAM_ERSST5 produces consistently smaller error metrics than CCAM_OISST across all prescribed minimum standard metrics within the benchmarking framework proposed by Isphording et al. (2023). Notably, OISST, characterized by high spatial and temporal resolution blending with satellite data, was initially anticipated to yield improved simulated regional rainfall when employed as a boundary condition for AGCM, in comparison to ERSST5. Our results have also revealed that CCAM tends to simulate a wet Australia. Therefore, advanced model evaluations are required to understand why CCAM_ERSST5 reduces the overestimation of rainfall amount over Australia.

Our findings underscore the inadequacy of relying on minimum standard metrics for ranking model outputs. While the conventional model evaluation approach favours CCAM_ERSST5 over CCAM_OISST based on these metrics, further examination reveals that CCAM_OISST outperforms CCAM_ERSST5 in replicating ENSO- and IOD-driven rainfall. As elucidated in Isphording et al. (2023), metrics within a benchmarking framework serve as binary indicators, filtering out simulations that fail to meet predefined performance expectations. For instance, we established a passing threshold for the mean absolute percentage bias (MAPE) in annual rainfall climatology at 0.7, designating simulations with a MAPE exceeding this threshold as unsuitable for further application. Both CCAM_OISST and CCAM_ERSST5 surpass the minimum standard metrics, indicating their capability in capturing basic Australian rainfall characteristics. However, the application of these models for specific purposes necessitates more targeted metrics. In our case, the evaluation of ENSO- and IOD-driven rainfall correlation, as highlighted in this paper, reveals the deficiency of CCAM_ERSST5 in reproducing these patterns over Australia. Consequently, CCAM_ERSST5 may not be suitable for ENSO/IOD-Australian rainfall studies. This result aligns with the perspective emphasized by Isphording et al. (2023) that the inclusion of more versatile metrics is essential in benchmarking simulations for specific fields of research. A collaborative effort within the climate research community is crucial to establish a consensus on prior performance expectations, or the passing thresholds of metrics, across diverse regions and aspects. Fostering a more robust and standardized benchmarking framework will help mitigate inconsistencies and subjectivity in assessing model performance.

4.2 Uncertainty of assessing model performance in IOD-rainfall

Some studies have found some disagreement between paleoclimate proxy records and observed long-term SST products (e.g., Abram et al. 2020, Pfeiffer et al. 2022), suggesting that considerable uncertainty of IOD variability might exist in long-term SST observations. This uncertainty is primarily attributed to the limited frequency and spatial coverage of observations from ships and buoys, particularly in the Southern Hemisphere and over the Indian Ocean (Freeman et al. 2017, Gopika et al. 2020). The scarcity of in situ observations introduces ambiguity into our understanding of IOD variability and, consequently, hinders an accurate representation of the IOD’s teleconnection with Australian rainfall. While the availability of satellite observations since the 1980s offers a valuable means to mitigate the uncertainty associated with IOD variability, the temporal coverage of satellite products is relatively short in the context of the IOD's characteristic timescales. This limitation is exacerbated by the relatively weak impact of IOD on Australian mean rainfall, with a correlation coefficient in the range of -0.3 to -0.4, as illustrated in Fig. 7. A robust analysis of the IOD's contribution to regional weather hence necessitates a sufficient number of IOD cases under diverse conditions. The limitations in data quality and spatiotemporal coverage of SST records thus add uncertainty in determining whether a climate model can replicate the observed IOD-rainfall relationship.

Apart from that, the overlapping influence of ENSO and IOD adds complexity to rainfall variability and extremes in Australia. In fact, ENSO and IOD often occur at the same time with the same phase (Abram et al. 2020). The correlation between monthly NINO3.4 and DMI in OISST is 0.6 during SON for the 1981-2020 period. The co-occurrence of ENSO and IOD can affect the remote impacts on local weather (e.g., Ashok et al. 2001, Cai et al. 2011, Ummenhofer et al. 2011). In the Australian context, the impacts of ENSO and IOD on rainfall often coexist (see Figs. 6 and 7). Consequently, the observed IOD-induced Australian rainfall may be partially attributed to ENSO. This interdependence implies that the observed relationship between IOD and rainfall is highly correlated to variations in ENSO, posing a challenge to the evaluation of model performance in capturing IOD-rainfall teleconnections.

IOD and its associated impacts display robust internal variability. Model experiments indicate that even a minor perturbation in initial conditions can lead to a substantial spread in IOD patterns and their correlated rainfall outcomes (Ng et al. 2018, Bodman et al. 2020). Consequently, it is plausible that the observed IOD-rainfall relationship represents just one realization among multiple potential impacts of the IOD. Moreover, the pronounced interdecadal variability of the IOD (Lim et al. 2017) introduces additional uncertainty into the assessment of observed IOD impacts. This is exemplified by the weak correlation between the DMI and Australian rainfall reported by Cai et al. (2011) for the period 1979-2008, wherein significant correlations, around -0.3, are primarily confined to Southeast Australia, with correlations elsewhere seldom stronger than -0.2. Contrastingly, during the period 1982-2022, as illustrated in Figure 7a, a markedly stronger correlation is observed across most of Australia. Notably, this intensified IOD-rainfall signal is predominantly contributed by the post-2000 period. Consequently, the reliability of IOD-rainfall teleconnections remains highly uncertain in the absence of sufficiently long-term and accurate SST and rainfall records. This prevailing uncertainty poses challenges in evaluating a model's ability to replicate the IOD-rainfall relationship, particularly when confidence in the observed IOD impacts remains low.

5 Conclusion

Our investigation utilizes the benchmarking framework proposed by Isphording et al. (2023) to assess the suitability of the variable-resolution AGCM, CCAM, for ENSO/IOD-rainfall research over Australia. We examine CCAM simulations driven by high-resolution OISST at 0.25° (CCAM_OISST) and low-resolution ERSST5 at 2° (CCAM_ERSST5). Both CCAM_OISST and CCAM_ERSST5 meet prior performance expectations in terms of minimum standards of basic rainfall characteristics, including rainfall climatology, seasonality and annual trends. However, both simulations tend to overestimate mean rainfall across most of Australia, with CCAM_OISST displaying a more pronounced overestimation than CCAM_ERSST5. Further verification of CCAM simulations in SON ENSO/IOD-rainfall reveals that only CCAM_OISST can replicate a realistic ENSO/IOD-rainfall relationship. Large differences in seasonal mean SST values, reaching up to 1K, between OISST and ERSST5 are found along the Australian coastline after spatial interpolation by CCAM. One potential contributor to this "Coastal Effect" is the dissimilarity in spatial resolution between the model and the driving SST. To further investigate this effect, an additional CCAM experiment, involving the replacement of SST values within a 5° proximity around the Australian continent in OISST with those from ERSST5 after spatial interpolation, underscores the sensitivity of IOD-induced rainfall to the "Coastal Effect". As a result, an accurate representation of local SST is important for model simulations in reproducing realistic IOD-rainfall responses over Australia. Moreover, climate model simulations with a considerable discrepancy in spatial resolutions between the model and the driving SST should be used with caution when analysing the impact of IOD on Australian rainfall.

Acknowledgements

This work was supported by the Australian Research Council (ARC) Grant CE170100023. YLL and LVA are also supported by ARC Grant FT210100459. This research was undertaken with the assistance of resources and services from the National Computational Infrastructure (NCI), which is supported by the Australian Government. We also thank Rachael Isphording for her substantial support in metric computation and graphical visualization for the assessment of CCAM based on the benchmarking framework suggested in Isphording et al. (2023) and Isphording (2023).

Open Research

OISST version 2.1 (Huang et al. 2021) used in this study is available from https://www.psl.noaa.gov/data/gridded/data.noaa.oisst.v2.highres.html. ERSST version 5 (Huang et al. 2017) used in this study is available from https://www.ncei.noaa.gov/pub/data/cmb/ersst/v5/netcdf/. ERA5 (Hersbach et al. 2020) used in this study is available from https://doi.org/10.24381/cds.bd0915c6 and the interpolated data initiating CCAM simulations is available on the National Computational Infrastructure Australia (NCI Australia) server in project xv83. AGCD (Evans et al. 2020) used in this study is available on the NCI Australia server in project zv2. CCAM is fully available from https://research.csiro.au/ccam/ while the version 2301 used in this study is also available on the NCI Australia server in project w42. All CCAM post-processed outputs used in this study are available on NCI Australia server in project w40. Registration for the NCI Australia and memberships of the corresponding projects are required. All data/model used in this study can be provided specifically upon request.

Code availability: Climpact (Alexander and Herold 2016) used in this study is available from https://climpact-sci.org/. Codes for pre-processing driving data and post-processing raw outputs of CCAM simulations are available from https://research.csiro.au/ccam/software-and-model-configuration/. Codes for benchmarking the CCAM's performance (Isphording 2023) are available from https://doi.org/10.5281/zenodo.8365065.

References

Abram, N. J., Hargreaves, J. A., Wright, N. M., Thirumalai, K., Ummenhofer, C. C., & England, M. H. (2020). Palaeoclimate perspectives on the Indian Ocean Dipole. *Quaternary Science Reviews*, *237*, 106302. https://doi.org/10.1016/j.quascirev.2020.106302

Alexander, L., & Herold, N. (2016). ClimPACT2: Indices and software. A document prepared on behalf of the Commission for Climatology (CCl) Expert Team on Sector-Specific Climate Indices (ET-SCI). https://epic.awi.de/id/eprint/49274/1/ClimPACTv2_manual.pdf

Ashok, K., Guan, Z., & Yamagata, T. (2001). Impact of the Indian Ocean dipole on the relationship between the Indian monsoon rainfall and ENSO. *Geophysical Research Letters*, *28*(23), 4499–4502. https://doi.org/10.1029/2001GL013294

Australian Bureau of Meteorology. (2021, March). *What is Niño and how does it impact Australia?*. http://www.bom.gov.au/climate/updates/articles/a008-el-nino-and-australia.shtml

Bamston, A. G., Chelliah, M., & Goldenberg, S. B. (1997). Documentation of a highly ENSO-related sst region in the equatorial pacific: Research note. *Atmosphere-Ocean*, *35*(3), 367–383. https://doi.org/10.1080/07055900.1997.9649597

Bodman, R. W., Karoly, D. J., Dix, M. R., Harman, I. N., Srbinovsky, J., Dobrohotoff, P. B., & Mackallah, C. (2020). Evaluation of CMIP6 AMIP climate simulations with the ACCESS-AM2 model. *Journal of Southern Hemisphere Earth Systems Science*, *70*(1), 166–179. https://doi.org/10.1071/ES19033

Boulard, D., Pohl, B., Crétat, J., Vigaud, N., & Pham-Xuan, T. (2013). Downscaling large-scale climate variability using a regional climate model: The case of ENSO over Southern Africa. *Climate Dynamics*, *40*(5–6), 1141–1168. https://doi.org/10.1007/s00382-012-1400-6

Cai, W., van Rensch, P., Cowan, T., & Hendon, H. H. (2011). Teleconnection pathways of ENSO and the IOD and the mechanisms for impacts on Australian rainfall. *Journal of Climate*, *24*(15), 3910–3923. https://doi.org/10.1175/2011JCLI4129.1

Cassola, F., Ferrari, F., Mazzino, A., & Miglietta, M. M. (2016). The role of the sea on the flash floods events over Liguria (northwestern Italy). *Geophysical Research Letters*, *43*(7), 3534–3542. https://doi.org/10.1002/2016GL068265

Castro, C. L., Pielke, R. A., & Leoncini, G. (2005). Dynamical downscaling: Assessment of value retained and added using the Regional Atmospheric Modeling System (RAMS). *Journal of Geophysical Research: Atmospheres*, *110*(D5), 2004JD004721. https://doi.org/10.1029/2004JD004721

Chapman, S., Syktus, J., Trancoso, R., Salazar, A., Thatcher, M., Watson, J. E. M., Meijaard, E., Sheil, D., Dargusch, P., & McAlpine, C. A. (2020). Compounding impact of deforestation on Borneo’s climate during El Niño events. *Environmental Research Letters*, *15*(8), 084006. https://doi.org/10.1088/1748-9326/ab86f5

Chen, X., Wu, P., Roberts, M. J., & Zhou, T. (2018). Potential Underestimation of Future Mei-Yu Rainfall with Coarse-Resolution Climate Models. *Journal of Climate*, *31*(17), 6711–6727. https://doi.org/10.1175/JCLI-D-17-0741.1

Chouinard, C., Béland, M., & McFarlane, N. (1986). A simple gravity wave drag parametrization for use in medium-range weather forecast models. *Atmosphere-Ocean*, *24*(2), 91–110. https://doi.org/10.1080/07055900.1986.9649242

Coates, L., Haynes, K., Gissing, A., & Radford, D. (2014). The Australian Experience and the Queensland Floods of 2010–2011. In J. J. L. M. Bierens (Ed.), *Drowning* (pp. 1075–1084). Springer Berlin Heidelberg. https://doi.org/10.1007/978-3-642-04253-9_162

Davey, S. M., & Sarre, A. (2020). Editorial: The 2019/20 Black Summer bushfires. *Australian Forestry*, *83*(2), 47–51. https://doi.org/10.1080/00049158.2020.1769899

Dechpichai, P., Jinapang, N., Yamphli, P., Polamnuay, S., Injan, S., & Humphries, U. (2022). Multivariable Panel Data Cluster Analysis of Meteorological Stations in Thailand for ENSO Phenomenon. *Mathematical and Computational Applications*, *27*(3), 37. https://doi.org/10.3390/mca27030037

Di Virgilio, G., Evans, J. P., Di Luca, A., Olson, R., Argüeso, D., Kala, J., Andrys, J., Hoffmann, P., Katzfey, J. J., & Rockel, B. (2019). Evaluating reanalysis-driven CORDEX regional climate models over Australia: Model performance and errors. *Climate Dynamics*, *53*(5–6), 2985–3005. https://doi.org/10.1007/s00382-019-04672-w

Evans, A., Jones, D., Lellyett, S., & Smalley, R. (2020). *An enhanced gridded rainfall analysis scheme for Australia*. Australian Bureau of Meteorology.

Evans, J. P., Bormann, K., Katzfey, J., Dean, S., & Arritt, R. (2016). Regional climate model projections of the South Pacific Convergence Zone. *Climate Dynamics*, *47*(3–4), 817–829. https://doi.org/10.1007/s00382-015-2873-x

Freeman, E., Woodruff, S. D., Worley, S. J., Lubker, S. J., Kent, E. C., Angel, W. E., Berry, D. I., Brohan, P., Eastman, R., Gates, L., Gloeden, W., Ji, Z., Lawrimore, J., Rayner, N. A., Rosenhagen, G., & Smith, S. R. (2017). ICOADS Release 3.0: A major update to the historical marine climate record. *International Journal of Climatology*, *37*(5), 2211–2232. https://doi.org/10.1002/joc.4775

Freidenreich, S. M., & Ramaswamy, V. (1999). A new multiple-band solar radiative parameterization for general circulation models. *Journal of Geophysical Research: Atmospheres*, *104*(D24), 31389–31409. https://doi.org/10.1029/1999JD900456

Gibson, P. B., Stone, D., Thatcher, M., Broadbent, A., Dean, S., Rosier, S. M., Stuart, S., & Sood, A. (2023). High-Resolution CCAM Simulations Over New Zealand and the South Pacific for the Detection and Attribution of Weather Extremes. *Journal of Geophysical Research: Atmospheres*, *128*(14), e2023JD038530. https://doi.org/10.1029/2023JD038530

Giorgi, F. (2019). Thirty Years of Regional Climate Modeling: Where Are We and Where Are We Going next? *Journal of Geophysical Research: Atmospheres*, *124*(11), 5696–5723. https://doi.org/10.1029/2018JD030094

Giorgi, F., & Gutowski, W. J. (2015). Regional Dynamical Downscaling and the CORDEX Initiative. *Annual Review of Environment and Resources*, *40*(1), 467–490. https://doi.org/10.1146/annurev-environ-102014-021217

Gillett, Z. E., Hendon, H. H., Arblaster, J. M., Lin, H., & Fuchs, D. (2022). On the Dynamics of Indian Ocean Teleconnections into the Southern Hemisphere during Austral Winter. *Journal of the Atmospheric Sciences*. https://doi.org/10.1175/JAS-D-21-0206.1

Gopika, S., Izumo, T., Vialard, J., Lengaigne, M., Suresh, I., & Kumar, M. R. R. (2020). Aliasing of the Indian Ocean externally-forced warming spatial pattern by internal climate variability. *Climate Dynamics*, *54*(1–2), 1093–1111. https://doi.org/10.1007/s00382-019-05049-9

Hamed, K. H. (2008). Trend detection in hydrologic data: The Mann–Kendall trend test under the scaling hypothesis. *Journal of Hydrology*, *349*(3–4), 350–363. https://doi.org/10.1016/j.jhydrol.2007.11.009

Hersbach, H., Bell, B., Berrisford, P., Hirahara, S., Horányi, A., Muñoz-Sabater, J., Nicolas, J., Peubey, C., Radu, R., Schepers, D., Simmons, A., Soci, C., Abdalla, S., Abellan, X., Balsamo, G., Bechtold, P., Biavati, G., Bidlot, J., Bonavita, M., … Thépaut, J. (2020). The ERA5 global reanalysis. *Quarterly Journal of the Royal Meteorological Society*, *146*(730), 1999–2049. https://doi.org/10.1002/qj.3803

Huang, B., Thorne, P. W., Banzon, V. F., Boyer, T., Chepurin, G., Lawrimore, J. H., Menne, M. J., Smith, T. M., Vose, R. S., & Zhang, H.-M. (2017). Extended Reconstructed Sea Surface Temperature, Version 5 (ERSSTv5): Upgrades, Validations, and Intercomparisons. *Journal of Climate*, *30*(20), 8179–8205. https://doi.org/10.1175/JCLI-D-16-0836.1

Huang, B., Liu, C., Banzon, V., Freeman, E., Graham, G., Hankins, B., Smith, T., & Zhang, H.-M. (2021). Improvements of the Daily Optimum Interpolation Sea Surface Temperature (DOISST) Version 2.1. *Journal of Climate*, *34*(8), 2923–2939. https://doi.org/10.1175/JCLI-D-20-0166.1

Huang, D., Yan, P., Zhu, J., Zhang, Y., Kuang, X., & Cheng, J. (2018). Uncertainty of global summer precipitation in the CMIP5 models: A comparison between high-resolution and low-resolution models. *Theoretical and Applied Climatology*, *132*(1–2), 55–69. https://doi.org/10.1007/s00704-017-2078-9

Hurley, P. (2007). Modelling Mean and Turbulence Fields in the Dry Convective Boundary Layer with the Eddy-Diffusivity/Mass-Flux Approach. *Boundary-Layer Meteorology*, *125*(3), 525–536. https://doi.org/10.1007/s10546-007-9203-8

Ishii, M., Shouji, A., Sugimoto, S., & Matsumoto, T. (2005). Objective analyses of sea-surface temperature and marine meteorological variables for the 20th century using

ICOADS and the Kobe Collection. *International Journal of Climatology*, *25*(7), 865–879. https://doi.org/10.1002/joc.1169

Isphording, R. N., 2023: aus_precip_benchmarking: Benchmarking Precipitation in Regional Climate Models: Jupyter Notebooks (Python) (v1.0). *Zenodo*. https://doi.org/10.5281/zenodo.8365065.

Isphording, R. N., Alexander, L. V., Bador, M., Green, D., Evans, J. P., & Wales, S. (2023). A Standardized Benchmarking Framework to Assess Downscaled Precipitation Simulations. *Journal of Climate (published online ahead of print 2023)*. https://doi.org/10.1175/JCLI-D-23-0317.1

Kara, A. B., Barron, C. N., Wallcraft, A. J., Oguz, T., & Casey, K. S. (2008). Advantages of fine resolution SSTs for small ocean basins: Evaluation in the Black Sea. *Journal of Geophysical Research: Oceans*, *113*(C8), 2007JC004569. https://doi.org/10.1029/2007JC004569

Katzfey, J., Nguyen, K., McGregor, J., Hoffmann, P., Ramasamy, S., Nguyen, H. V., Khiem, M. V., Nguyen, T. V., Truong, K. B., Vu, T. V., Nguyen, H. T., Thuc, T., Phong, D. H., Nguyen, B. T., Phan-Van, T., Nguyen-Quang, T., Ngo-Duc, T., & Trinh-Tuan, L. (2016). High-resolution simulations for Vietnam—Methodology and evaluation of current climate. *Asia-Pacific Journal of Atmospheric Sciences*, *52*(2), 91–106. https://doi.org/10.1007/s13143-016-0011-2

Kotwicki, V., & Allan, R. (1998). La Niña de Australia—Contemporary and palaeo-hydrology of Lake Eyre. *Palaeogeography, Palaeoclimatology, Palaeoecology*, *144*(3–4), 265–280. https://doi.org/10.1016/S0031-0182(98)00122-9

Kowalczyk, E. A., Wang, Y. P., Law, R. M., Davies, H. L., McGregor, J. L., & Abramowitz, G. (2006). *The CSIRO Atmosphere Biosphere Land Exchange (CABLE) model for use in climate models and as an offline model*. https://doi.org/10.1016/j.agsy.2016.07.001

Lim, E.-P., Hudson, D., Wheeler, M. C., Marshall, A. G., King, A., Zhu, H., Hendon, H. H., De Burgh-Day, C., Trewin, B., Griffiths, M., Ramchurn, A., & Young, G. (2021). Why Australia was not wet during spring 2020 despite La Niña. *Scientific Reports*, *11*(1), 18423. https://doi.org/10.1038/s41598-021-97690-w

Lin, Y.-L., Farley, R. D., & Orville, H. D. (1983). Bulk Parameterization of the Snow Field in a Cloud Model. *Journal of Climate and Applied Meteorology*, *22*(6), 1065–1092. https://doi.org/10.1175/1520-0450(1983)022<1065:BPOTSF>2.0.CO;2

Liu, J., Zhang, Y., Yang, Y., Gu, X., & Xiao, M. (2018). Investigating Relationships Between Australian Flooding and Large-Scale Climate Indices and Possible Mechanism. *Journal of Geophysical Research: Atmospheres*, *123*(16), 8708–8723. https://doi.org/10.1029/2017JD028197

Madden, R. A., & Julian, P. R. (1971). Detection of a 40–50 Day Oscillation in the Zonal Wind in the Tropical Pacific. *Journal of the Atmospheric Sciences*, *28*(5), 702–708. https://doi.org/10.1175/1520-0469(1971)028<0702:DOADOI>2.0.CO;2

Madden, R. A., & Julian, P. R. (1972). Description of Global-Scale Circulation Cells in the Tropics with a 40–50 Day Period. *Journal of the Atmospheric Sciences*, *29*(6), 1109–1123. https://doi.org/10.1175/1520-0469(1972)029<1109:DOGSCC>2.0.CO;2

Mantegna, G. A., White, C. J., Remenyi, T. A., Corney, S. P., & Fox-Hughes, P. (2017). Simulating sub-daily Intensity-Frequency-Duration curves in Australia using a dynamical high-resolution regional climate model. *Journal of Hydrology*, *554*, 277–291. https://doi.org/10.1016/j.jhydrol.2017.09.025

Marbaix, P., Gallée, H., Brasseur, O., & Van Ypersele, J.-P. (2003). Lateral Boundary Conditions in Regional Climate Models: A Detailed Study of the Relaxation Procedure. *Monthly Weather Review*, *131*(3), 461–479. https://doi.org/10.1175/1520-0493(2003)131<0461:LBCIRC>2.0.CO;2

McGregor, J. L. (2003). A new convection scheme using a simple closure. *CSIRO Atmospheric Research*, PB1 Aspendale, Vic. 3195, Australia.

McGregor, J. L. (2005). Geostrophic Adjustment for Reversibly Staggered Grids. *Monthly Weather Review*, *133*(5), 1119–1128. https://doi.org/10.1175/MWR2908.1

McGregor, J. L. (2015). Recent developments in variable-resolution global climate modelling. *Climatic Change*, *129*(3–4), 369–380. https://doi.org/10.1007/s10584-013-0866-5

McGregor, J. L. (2005). *C-CAM : geometric aspects and dynamical formulation*. CSIRO Atmospheric Research, Aspendale, Vic. 3195, Australia.

McGregor, J.L., Dix, M.R. (2008). An Updated Description of the Conformal-Cubic Atmospheric Model. In: Hamilton, K., Ohfuchi, W. (eds) *High Resolution Numerical Modelling of the Atmosphere and Ocean*. Springer, New York, NY. https://doi.org/10.1007/978-0-387-49791-4_4

Meyers, G., McIntosh, P., Pigot, L., & Pook, M. (2007). The years of El Niño, La Niña and interactions with the tropical Indian Ocean. *Journal of Climate*, *20*(13), 2872–2880. https://doi.org/10.1175/JCLI4152.1

Ng, B., Cai, W., Cowan, T., & Bi, D. (2018). Influence of internal climate variability on Indian Ocean Dipole properties. *Scientific Reports*, *8*(1), 1–8. https://doi.org/10.1038/s41598-018-31842-3

Nurlatifah, A., Sipayung, S. B., & Siswanto, B. (2019). Rainfall Scenario of West Nusa Tenggara in 2040 Based on CCAM RCP 4.5. *IOP Conference Series: Earth and*

Environmental Science, *303*(1), 012033. https://doi.org/10.1088/1755-1315/303/1/012033

Pfeiffer, M., Watanabe, T. K., Takayanagi, H., Cahyarini, S. Y., Garbe-Schönberg, D., & Watanabe, T. (2022). Coral Sr/Ca records provide realistic representation of eastern Indian Ocean cooling during extreme positive Indian Ocean Dipole events. *Scientific Reports*, *12*(1), 10642. https://doi.org/10.1038/s41598-022-14617-9

Ratna, S. B., Ratnam, J., Behera, S., Tangang, F., & Yamagata, T. (2017). Validation of the WRF regional climate model over the subregions of Southeast Asia: Climatology and interannual variability. *Climate Research*, *71*(3), 263–280. https://doi.org/10.3354/cr01445

Ratna, S. B., Cherchi, A., Osborn, T. J., Joshi, M., & Uppara, U. (2021). The Extreme Positive Indian Ocean Dipole of 2019 and Associated Indian Summer Monsoon Rainfall Response. *Geophysical Research Letters*, *48*(2), e2020GL091497. https://doi.org/10.1029/2020GL091497

Rauscher, S. A., Coppola, E., Piani, C., & Giorgi, F. (2010). Resolution effects on regional climate model simulations of seasonal precipitation over Europe. *Climate Dynamics*, *35*(4), 685–711. https://doi.org/10.1007/s00382-009-0607-7

Rayner, N. A. (2003). Global analyses of sea surface temperature, sea ice, and night marine air temperature since the late nineteenth century. *Journal of Geophysical Research*, *108*(D14), 4407. https://doi.org/10.1029/2002JD002670

Rotstayn, L. D. (1997). A physically based scheme for the treatment of stratiform clouds and precipitation in large-scale models. I: Description and evaluation of the microphysical processes. *Quarterly Journal of the Royal Meteorological Society*, *123*(541), 1227–1282. https://doi.org/10.1002/qj.49712354106

Rotstayn, L. D., Collier, M. A., Mitchell, R. M., Qin, Y., Campbell, S. K., & Dravitzki, S. M. (2011). Simulated enhancement of ENSO-related rainfall variability due to Australian dust. *Atmospheric Chemistry and Physics*, *11*(13), 6575–6592. https://doi.org/10.5194/acp-11-6575-2011

Rotstayn, L. D., & Lohmann, U. (2002). Simulation of the tropospheric sulfur cycle in a global model with a physically based cloud scheme: SULFUR CYCLE IN A GLOBAL MODEL. *Journal of Geophysical Research: Atmospheres*, *107*(D21), AAC 20-1-AAC 20-21. https://doi.org/10.1029/2002JD002128

Saji, N. H., Goswami, B. N., Vinayachandran, P. N., &Yamagata, T. (1999). A dipole mode in the tropical Indian Ocean. *Nature*, *401*, 360–363. https://doi.org/https://doi.org/10.1038/43854

Saji, N. H., & Yamagata, T. (2003). Possible impacts of Indian Ocean Dipole mode events on global climate. *CLIMATE RESEARCH Clim Res*, *25*, 151–169. http://dx.doi.org/10.3354/cr025151

Safari, B., Sebaziga, J. N., & Siebert, A. (2023). Evaluation of CORDEX-CORE regional climate models in simulating rainfall variability in Rwanda. *International Journal of Climatology*, *43*(2), 1112–1140. https://doi.org/10.1002/joc.7891

Schmidt, F. (1977), Variable fine mesh in spectral global model, *Beitr. Phys. Atmos*, *50*, 211–217.

Schwarzkopf, M. D., & Ramaswamy, V. (1999). Radiative effects of CH_4, N_2O, halocarbons and the foreign-broadened H_2O continuum: A GCM experiment. *Journal of Geophysical Research: Atmospheres*, *104*(D8), 9467–9488. https://doi.org/10.1029/1999JD900003

Tapiador, F. J., Navarro, A., Moreno, R., Sánchez, J. L., & García-Ortega, E. (2020). Regional climate models: 30 years of dynamical downscaling. *Atmospheric Research*, *235*, 104785. https://doi.org/10.1016/j.atmosres.2019.104785

Thatcher, M., & McGregor, J. L. (2011). A Technique for Dynamically Downscaling Daily-Averaged GCM Datasets Using the Conformal Cubic Atmospheric Model. *Monthly Weather Review*, *139*(1), 79–95. https://doi.org/10.1175/2010MWR3351.1

Thatcher, M., Rafter, T., Truong, S., Trenham, C., McGregor, J. L., & Katzfey, J. (2023, Feburary). *CCAM documentations*. https://confluence.csiro.au/display/CCAM/CCAM

Toersilowati, L., Siswanto, B., Maryadi, E., Susanti, I., Suhermat, M., Witono, A., Sipayung, S. B., Rahayu, S. A., ‘Adany, F., Aminuddin, J., & Lubis, R. F. (2022). The Projections of Climate Change using Conformal Cubic Atmospheric Model (CCAM) in Bali—Indonesia. *IOP Conference Series: Earth and Environmental Science*, *1047*(1), 012033. https://doi.org/10.1088/1755-1315/1047/1/012033

Trenberth, K. E. (1997). The Definition of El Niño. *Bulletin of the American Meteorological Society*, *78*(12), 2771–2777. https://doi.org/10.1175/1520-0477(1997)078<2771:TDOENO>2.0.CO;2

Ummenhofer, C. C., England, M. H., Mclntosh, P. C., Meyers, G. A., Pook, M. J., Risbey, J. S., Gupta, A. S., & Taschetto, A. S. (2009). What causes southeast Australia’s worst droughts? *Geophysical Research Letters*, *36*(4). https://doi.org/10.1029/2008GL036801

Verma, S., & Bhatla, R. (2021). Performance of RegCM4 for Dynamically Downscaling of El Nino/La Nina Events During Southwest Monsoon Over India and Its Regions. *Earth and Space Science*, *8*(3), e2020EA001474. https://doi.org/10.1029/2020EA001474

Verdon-Kidd, D. C. (2018). On the classification of different flavours of Indian Ocean Dipole events. *International Journal of Climatology*, *38*(13), 4924–4937. https://doi.org/10.1002/joc.5707

Wang, G., & Hendon, H. H. (2007). Sensitivity of Australian Rainfall to Inter–El Niño Variations. Journal of Climate, 20(16), 4211–4226. https://doi.org/10.1175/JCLI4228.1

Whan, K., & Zwiers, F. (2017). The impact of ENSO and the NAO on extreme winter precipitation in North America in observations and regional climate models. *Climate Dynamics*, *48*(5–6), 1401–1411. https://doi.org/10.1007/s00382-016-3148-x

Worku, G., Teferi, E., Bantider, A., Dile, Y. T., & Taye, M. T. (2018). Evaluation of regional climate models performance in simulating rainfall climatology of Jemma sub-basin, Upper Blue Nile Basin, Ethiopia. *Dynamics of Atmospheres and Oceans*, *83*, 53–63. https://doi.org/10.1016/j.dynatmoce.2018.06.002